Strain smoothing for compressible and nearly-incompressible finite elasticity

Chang-Kye Lee [a], L. Angela Mihai [b], Jack S. Hale [c], Pierre Kerfriden [a], Stéphane P.A. Bordas [c,a,*]

[a] *Cardiff School of Engineering, Cardiff University, The Queen's Building, The Parade, Cardiff, Wales CF24 3AA, UK*
[b] *Cardiff School of Mathematics, Cardiff University, Senghennydd Road, Cardiff, Wales CF24 4AG, UK*
[c] *Université du Luxembourg, Faculté des Sciences, de la Technologies et de la Communication, Campus Kirchberg, 6, rue Coudenhove-Kalergi, L-1359, Luxembourg*

ABSTRACT

We present a robust and efficient form of the smoothed finite element method (S-FEM) to simulate hyperelastic bodies with compressible and nearly-incompressible neo-Hookean behaviour. The resulting method is stable, free from volumetric locking and robust on highly distorted meshes. To ensure inf-sup stability of our method we add a cubic bubble function to each element. The weak form for the smoothed hyperelastic problem is derived analogously to that of smoothed linear elastic problem. Smoothed strains and smoothed deformation gradients are evaluated on sub-domains selected by either edge information (edge-based S-FEM, ES-FEM) or nodal information (node-based S-FEM, NS-FEM). Numerical examples are shown that demonstrate the efficiency and reliability of the proposed approach in the nearly-incompressible limit and on highly distorted meshes. We conclude that, strain smoothing is at least as accurate and stable, as the MINI element, for an equivalent problem size.

1. Introduction

Low-order simplex (triangular or tetrahedral) finite element methods (FEM) are widely used because of computational efficiency, simplicity of implementation and the availability of largely automatic mesh generation for complex geometries. However, the accuracy of the low-order simplex FEM suffers in the incompressible limit, an issue commonly referred to as volumetric locking, and also when the mesh becomes highly distorted.

To deal with these difficulties various numerical techniques have been developed. A classical approach is to use hexahedral elements instead of tetrahedral elements due to their superior performance in plasticity, nearly-incompressible and bending problems, and additionally their reduced sensitivity to highly distorted meshes. However, automatically generating high-quality conforming hexahedral meshes of complex geometries is still not possible, and for this reason it is desirable to develop improved methods that can use simplex meshes. Significant progress has, however, been done in this direction [1].

Another option is to move to higher-order polynomial simplex elements. While they are significantly better than linear tetrahedral elements in terms of accuracy this is at the expense of increased implementational and computational complexity, and sensitivity to distortion.

Nodally averaged simplex elements [2,3] can effectively deal with nearly-incompressible materials, but they still suffer from an overly stiff behaviour in certain cases [4].

Meshfree (or meshless) methods [5–7] are another option because of their improved accuracy on highly-distorted nodal layouts, but the locking problem is still a challenging issue that needs careful consideration [8]. To improve the non-mesh based methods, B-bar approach [9,10], which is appropriate not only to handle incompressible limits but also to model shear bands with cohesive surfaces, can be considered. Additionally, because they are substantially different to the FEM, they are not easily implemented in it existing software.

Isogeometric Analysis (IGA) is another high-order alternative and the interested reader is referred to [11,12]. Moreover for the further studies for fractures undergoing large deformations, edge rotation algorithm can be an another option in large plastic strains [13,14].

Mixed and enhanced formulations are another popular remedy for volumetric locking [15,16], but they retain the sensitivity to mesh distortion of the standard simplex FEM [17].

Another approach, and the one that we employ in this paper, is the strain smoothing method developed by Liu et al. [18,19]. The strain smoothing method has the advantage over the above methods that it improves both the behaviour of low-order simplex ele-

ments with respect to both volumetric locking and highly distorted meshes, while being simple to implement within an existing finite element code.

The basic idea of strain smoothing is based on the stabilised conforming nodal integration (SCNI) proposed in the context of meshfree methods by Chen et al. [20,21]. Later SCNI was extended to the natural element method (NEM) by Yoo et al. [22], and was shown to effectively handle nearly-incompressible problems.

In the smoothed finite element method (S-FEM), the domain is divided into smoothing domains where the strain is smoothed as shown in Fig. 1. Typically, the geometry of the smoothing domains is derived directly from the standard simplex mesh geometry. Then with the divergence theorem, numerical integration is transferred from the interior to the boundary of the smoothing domains [23,24]. Critically, this procedure results in a discrete weak form without the Jacobian, the matrix used to map basis function derivatives from the reference element to the real element in the mesh. In the standard FEM the Jacobian is required to construct the derivatives of the basis functions. When distorted meshes are used in the standard FEM, the Jacobian becomes ill-conditioned, and this affects the accuracy of the method. Because the Jacobian is not required in S-FEM, the resulting method is significantly more robust than the standard FEM on highly distorted meshes.

It is also known that the S-FEM produces stiffness matrices that are less stiff than the standard FEM, and in certain cases this property can be used to overcome volumetric locking. Since S-FEM was introduced, its properties have been studied from a theoretical viewpoint [18,19,25–29], extended to n-sided polygonal elements [30] and applied to many engineering problems such as plate and shell analysis [31–34].

Particularly, Bordas et al. [35] recalled the central theory and features of S-FEM and showed notable properties of S-FEM which depend on the number of smoothing domains in an element. Moreover, Bordas et al. [35] presented the coupling of strain smoothing and partition of unity enrichment, so called SmXFEM, with examples of cracks in linear elastic continua and arbitrary cracks in plates.

The contribution of this paper to the literature is to present a robust, efficient and stable form of the smoothed finite element methods to simulate both compressible and nearly-compressible hyperelastic bodies. We study two forms of smoothing (node-based and edge-based) and compare their relative merits. A key ingredient of our method is to add cubic bubbles to each element to ensure inf-sup stability. Although bubbles have been suggested before in the context of linear elastic S-FEM by Nguyen-Xuan and

Liu [36] here we make the non-trivial extension to deal with hyperelastic problems. Finally we present a rigorous testing procedure that demonstrates the superior performance of our approach over the standard FEM.

The outline of this paper is as follows; first, we briefly review the idea fundamentals of S-FEM. In Section 3 we formulate the non-linear S-FEM for hyperelastic neo-Hookean compressible materials. To demonstrate the accuracy and convergence properties of the proposed methods we present extensive benchmark tests in Section 4. Finally, conclusions and future work directions are summarised in Section 5.

2. Smoothed finite element method (S-FEM)

It was shown in numerous studies that S-FEM provides a higher efficiency, i.e. computational cost versus error than the conventional FEM for many mechanical problems. We list below some of the strengths and weaknesses of each variant: the cell-based smoothed FEM (CS-FEM), the edge-based smoothed FEM (ES-FEM), the node-based smoothed FEM (NS-FEM), and the face-based smoothed FEM (FS-FEM).

- **Volumetric locking**. NS-FEM can handle effectively nearly-incompressible materials where Poisson's ratio $v \rightarrow 0.5$ [37], while ES-FEM suffers from volumetric locking. Combining NS- and ES-FEM gives the so-called *the smoothing-domain-based selective ES/NS-FEM* which also overcomes volumetric locking [38]. In the case of CS-FEM, volumetric locking can be avoided by selective integration [39].
- **Upper and lower bound properties**. In typical engineering analysis with homogeneous Dirichlet boundary conditions the NS-FEM gives upper bound solution and FEM obtains lower bound solution in the energy norm. While, in the case of problem with no external force but non-homogeneous Dirichlet boundary conditions, NS-FEM and FEM provide lower and upper bounds in the energy norm, respectively [40,41].
- **Static and dynamic analyses**. ES-FEM gives accurate and stable results when solving either static or dynamic problems [42]. In contrast, although NS-FEM is spatially stable, it is temporally unstable. Therefore, to solve dynamic problems, NS-FEM requires stabilisation techniques [43,44]. CS-FEM can also be extended to solve dynamic problems [45].
- **Other features**. In NS-FEM, the accuracy of the solution in the displacement norm is comparable to that of the standard FEM using the same mesh, whereas the accuracy of stress solutions

(a) The smoothing domain for edge-based smoothed FEM (ES-FEM)

(b) The smoothing domain for node-based smoothed FEM (NS-FEM)
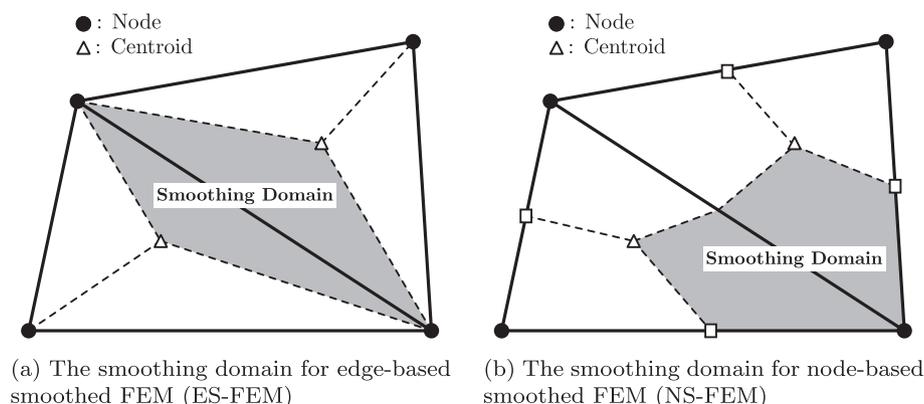
Fig. 1. (a) Three smoothing domains in the three-node triangular (T3) finite mesh for edge-based smoothed FEM (ES-FEM), (b) three smoothing domains in the three-node triangular (T3) finite mesh for node-based smoothed FEM (NS-FEM).

in the energy norm is superior to that of FEM [38]. In terms of computational time, in general, ES-FEM is more expensive than conventional FEM on the same mesh [38].

2.1. Non-linear elasticity and S-FEM approximation

The principle of virtual work for finite elasticity can be written in the Galerkin weak form [46–48]:

$$\int_\Omega \frac{\partial \mathcal{W}}{\partial \tilde{\mathbf{F}}}(\mathbf{X}, \tilde{\mathbf{F}}(\mathbf{u})) : \nabla \mathbf{v} \, d\Omega = \int_\Omega \mathbf{f} \cdot \mathbf{v} \, dV + \int_{\Gamma_N} \mathbf{g} \cdot \mathbf{v} \, dA \tag{1}$$

where the smoothed deformation gradient $\tilde{\mathbf{F}} = \mathbf{I} + \nabla \mathbf{u}$ is written in terms of displacements $\mathbf{u}$, $\mathbf{v}$ is the set of admissible test functions. The strain energy density function $\mathcal{W}$ for a compressible neo-Hookean material [49] is:

$$\mathcal{W} = \frac{1}{2}\lambda(\ln J)^2 - \mu \ln J + \frac{1}{2}\mu(\mathrm{tr}\mathbf{C} - 3) \tag{2}$$

where Lame's first parameter λ is $\lambda = k - \frac{2}{3}\mu$, and the shear modulus $\mu > 0$ and the bulk modulus $k > 0$ are material parameters.

The smoothed deformation gradient $\tilde{\mathbf{F}}$ for the proposed technique is:

$$\tilde{\mathbf{F}}(\mathbf{x}_k) = \frac{1}{A_k}\int_{\Omega_k} \mathbf{F}(\mathbf{x}_k)\Phi(\mathbf{x}_k)\,d\Omega \tag{3}$$

where the deformation gradient $\mathbf{F}$ is given in Appendix A.

To find an approximate solution using Eq. (2) for the displacement field $\mathbf{u}$, we employ the Newton-Raphson method. At iteration iter + 1, knowing the displacement $\mathbf{u}_{\mathrm{iter}}$ from iteration iter, find $\mathbf{r}_{\mathrm{iter}}$ that satisfies [46]:

$$D\mathcal{R}(\mathbf{u}_{\mathrm{iter}}) \cdot \mathbf{r}_{\mathrm{iter}} = -\mathcal{R}(\mathbf{u}_{\mathrm{iter}}) \tag{4}$$

where

$$\mathcal{R}(\mathbf{u}) = \int_\Omega \frac{\partial \mathcal{W}}{\partial \tilde{F}_{ij}}(\mathbf{x}, \tilde{\mathbf{F}}(\mathbf{u}))\frac{\partial v_i}{\partial X_j}\,dV - \int_\Omega f_i v_i\,dV - \int_{\Gamma_N} g_i v_i\,dA \tag{5}$$

$$D\mathcal{R}(\mathbf{u}) \cdot \mathbf{r} = \int_\Omega \frac{\partial^2 \mathcal{W}}{\partial \tilde{F}_{ij}\partial \tilde{F}_{kl}}(\mathbf{x}, \tilde{\mathbf{F}}(\mathbf{u}))\frac{\partial r_k}{\partial X_l}\frac{\partial v_i}{\partial X_j}\,dV \tag{6}$$

and $i, j, k, l \in \{1, 2\}$ for two dimensional problems.

The energy function Eq. (5) and its directional derivatives Eq. (6) become the following equivalent formulations, respectively:

$$\mathcal{R}(\mathbf{u}) = \int_\Omega 2\frac{\partial \mathcal{W}}{\partial \tilde{C}_{ij}}\tilde{F}_{ki}\frac{\partial v_k}{\partial X_j}\,dV - \int_\Omega f_i v_i\,dV - \int_{\Gamma_N} g_i v_i\,dA \tag{7}$$

$$D\mathcal{R}(\mathbf{u}) \cdot \mathbf{r} = \int_\Omega 4\frac{\partial^2 \mathcal{W}}{\partial \tilde{C}_{ij}\partial \tilde{C}_{kl}}\tilde{F}_{pi}\frac{\partial v_p}{\partial X_j}\tilde{F}_{sk}\frac{\partial r_s}{\partial X_l} + 2\frac{\partial \mathcal{W}}{\partial \tilde{C}_{ij}}\frac{\partial r_k}{\partial X_i}\frac{\partial v_k}{\partial X_j}\,dV \tag{8}$$

where $i, j, k, l, p, s \in \{1, 2\}$.

The resulting algebraic system for the numerical approximation of Eq. (4) is assembled from the block systems:

$$\begin{bmatrix} \tilde{K}_{11} & \tilde{K}_{12} \\ \tilde{K}_{12} & \tilde{K}_{22} \end{bmatrix}\begin{bmatrix} r_1 \\ r_2 \end{bmatrix} = \begin{bmatrix} \tilde{b}_1 \\ \tilde{b}_2 \end{bmatrix} \tag{9}$$

By taking $\mathbf{v} = \sum_I N_I v_I$, we obtain the stiffness matrix $\tilde{\mathbf{K}}_{\mathrm{iter}}$ with following components:

$$\tilde{K}_{11} = \int_\Omega 4\frac{\partial^2 \mathcal{W}}{\partial \tilde{C}_{ij}\partial \tilde{C}_{kl}}\left(\delta_{1i} + \frac{\partial u_1}{\partial X_i}\right)\frac{\partial N_1}{\partial X_j}\left(\delta_{1k} + \frac{\partial u_1}{\partial X_k}\right)\frac{\partial N_1}{\partial X_l} \\ + 2\frac{\partial \mathcal{W}}{\partial C_{ij}}\frac{\partial N_1}{\partial X_i}\frac{\partial N_1}{\partial X_j}\,dV$$

$$\tilde{K}_{12} = \int_\Omega 4\frac{\partial^2 \mathcal{W}}{\partial \tilde{C}_{ij}\partial \tilde{C}_{kl}}\left(\delta_{1i} + \frac{\partial u_1}{\partial X_i}\right)\frac{\partial N_1}{\partial X_i}\left(\delta_{2k} + \frac{\partial u_2}{\partial X_k}\right)\frac{\partial N_2}{\partial X_l}\,dV \tag{10}$$

$$\tilde{K}_{21} = \tilde{K}_{12}$$

$$\tilde{K}_{22} = \int_\Omega 4\frac{\partial^2 \mathcal{W}}{\partial \tilde{C}_{ij}\partial \tilde{C}_{kl}}\left(\delta_{2i} + \frac{\partial u_2}{\partial X_i}\right)\frac{\partial N_2}{\partial X_j}\left(\delta_{2k} + \frac{\partial u_2}{\partial X_k}\right)\frac{\partial N_2}{\partial X_l} \\ + 2\frac{\partial \mathcal{W}}{\partial C_{ij}}\frac{\partial N_2}{\partial X_i}\frac{\partial N_2}{\partial X_j}\,dV$$

and the components of the load vector are:

$$\tilde{b}_1 = -\int_\Omega 2\frac{\partial \mathcal{W}}{\partial C_{ij}}\left(\delta_{1i} + \frac{\partial u_1}{\partial X_i}\right)\frac{\partial N_1}{\partial X_j} + \int_\Omega f_1 N_1\,dV + \int_{\Gamma_N} g_1 N_1\,dA$$
$$\tilde{b}_2 = -\int_\Omega 2\frac{\partial \mathcal{W}}{\partial C_{ij}}\left(\delta_{2i} + \frac{\partial u_2}{\partial X_i}\right)\frac{\partial N_2}{\partial X_j} + \int_\Omega f_2 N_2\,dV + \int_{\Gamma_N} g_2 N_2\,dA \tag{11}$$

The smoothed tangent stiffness $\tilde{\mathbf{K}}^{\mathrm{tan}} = \tilde{\mathbf{K}}^{\mathrm{mat}} + \tilde{\mathbf{K}}^{\mathrm{geo}}$ can be re-written using Eq. (10):

$$\tilde{\mathbf{K}}^{\mathrm{mat}} = \int_\Omega \tilde{\mathbf{B}}_0^{\mathrm{T}}\tilde{\mathbb{C}}\tilde{\mathbf{B}}_0\,d\Omega = \sum_{k=1}^{N_e}\int_{\Omega_k}\tilde{\mathbf{B}}_0^{\mathrm{T}}\tilde{\mathbb{C}}\tilde{\mathbf{B}}_0\,d\Omega = \sum_{k=1}^{N_e}\tilde{\mathbf{B}}_0^{\mathrm{T}}\tilde{\mathbb{C}}\tilde{\mathbf{B}}_0 A_k$$

$$\tilde{\mathbf{K}}^{\mathrm{geo}} = \int_\Omega \tilde{\mathcal{B}}^{\mathrm{T}}\tilde{\mathbf{S}}\tilde{\mathcal{B}}\,d\Omega = \sum_{k=1}^{N_e}\int_{\Omega_k}\tilde{\mathcal{B}}^{\mathrm{T}}\tilde{\mathbf{S}}\tilde{\mathcal{B}}\,d\Omega = \sum_{k=1}^{N_e}\tilde{\mathcal{B}}^{\mathrm{T}}\tilde{\mathbf{S}}\tilde{\mathcal{B}} A_k \tag{12}$$

where the smoothed strain-displacement matrices $\tilde{\mathbf{B}}_0$ and $\tilde{\mathcal{B}}$ can be expressed respectively as (also see in Fig. 2)

$$\tilde{\mathbf{B}}_0(\mathbf{x}) = \begin{bmatrix} \tilde{\mathbf{B}}_{I1}\tilde{F}_{11} & \tilde{\mathbf{B}}_{I1}\tilde{F}_{21} \\ \tilde{\mathbf{B}}_{I2}\tilde{F}_{12} & \tilde{\mathbf{B}}_{I2}\tilde{F}_{22} \\ \tilde{\mathbf{B}}_{I2}\tilde{F}_{11} + \tilde{\mathbf{B}}_{I1}\tilde{F}_{12} & \tilde{\mathbf{B}}_{I1}\tilde{F}_{22} + \tilde{\mathbf{B}}_{I2}\tilde{F}_{21} \end{bmatrix} \tag{13a}$$

$$\tilde{\mathcal{B}}(\mathbf{x}) = \begin{bmatrix} \tilde{\mathbf{B}}_{I1} & 0 \\ \tilde{\mathbf{B}}_{I2} & 0 \\ 0 & \tilde{\mathbf{B}}_{I1} \\ 0 & \tilde{\mathbf{B}}_{I2} \end{bmatrix} \tag{13b}$$

and by Eq. (11) the load vector $\tilde{\mathbf{b}}$ is:

$$\tilde{\mathbf{b}} = \sum_{k=1}^{N_e}\tilde{\mathbf{B}}_0\{\tilde{\mathbf{S}}\}A_k \tag{14}$$

where matrix $\tilde{\mathbf{S}}$ is:

$$\tilde{\mathbf{S}} = \begin{bmatrix} \tilde{S}_{11} & \tilde{S}_{12} & 0 & 0 \\ \tilde{S}_{12} & \tilde{S}_{22} & 0 & 0 \\ 0 & 0 & \tilde{S}_{11} & \tilde{S}_{12} \\ 0 & 0 & \tilde{S}_{12} & \tilde{S}_{22} \end{bmatrix} \tag{15}$$

and

$$\{\tilde{\mathbf{S}}\} = \begin{Bmatrix} \tilde{S}_{11} \\ \tilde{S}_{22} \\ \tilde{S}_{12} \end{Bmatrix} \tag{16}$$

where the fourth-order elasticity tensor $\tilde{\mathbb{C}}$ is:

$$\tilde{\mathbb{C}} = \begin{bmatrix} \tilde{\mathbb{C}}_{11} & \tilde{\mathbb{C}}_{12} & 0 \\ \tilde{\mathbb{C}}_{12} & \tilde{\mathbb{C}}_{22} & 0 \\ 0 & 0 & \tilde{\mathbb{C}}_{66} \end{bmatrix} \tag{17}$$
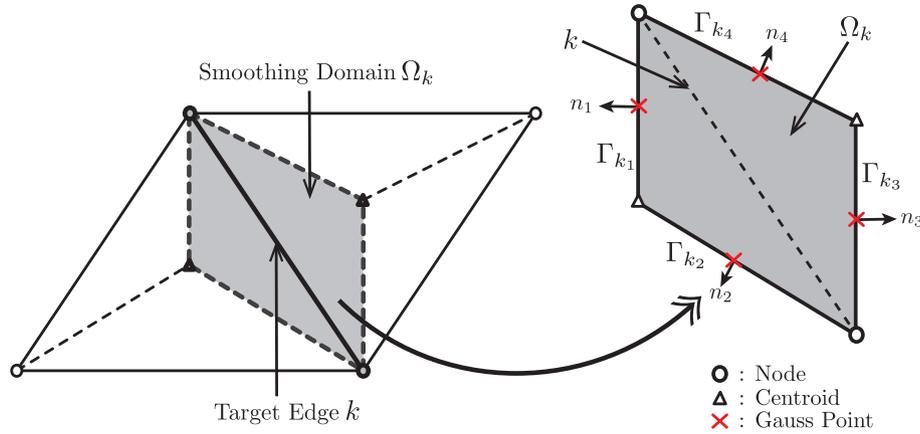
Fig. 2. The integration is performed on Gauss points located at the mid-point of the boundaries Γ_k of the smoothing domain Ω_k.

Finally, the global system of equations Eq. (4) can be written as:

$$\tilde{\mathbf{K}}_{\text{iter}}\mathbf{r}_{\text{iter}} = \tilde{\mathbf{b}}_{\text{iter}} \tag{18}$$

and

$$\mathbf{u}_{\text{iter}+1} = \mathbf{u}_{\text{iter}} + \mathbf{r}_{\text{iter}} \tag{19}$$

3. Enriched strain smoothing method with bubble functions

In the finite element method, to apply the Ritz-Galerkin method to a variational problem, a finite dimensional sub-space of space $\mathbb{V}$ is required. The space $\mathbb{V}$ defined on domain Ω is approximated by simple functions which are polynomials [50].

$$\mathbb{V} = \{\mathbf{u} \in (\mathbb{H}^1(\Omega))^2, \ \mathbf{u} = \mathbf{u}_\Gamma \text{ on } \Gamma_D\} \tag{20}$$

where displacement $\mathbf{u}$, boundary Γ and a Hilbert space $\mathbb{H}^1(\Omega)$. In this space, we cannot avoid the locking phenomenon in the incompressible limit, and S-FEM may face this obstacle as well because in both FEM and S-FEM, the same low-order simplex elements are used. One popular technique to overcome the locking effects is employing bubble functions within mixed finite element approximation [51,52]. Nguyen-Xuan and Liu [36] proposed a bubble enriched smoothed finite element method called the bES-FEM (see also [53]). In addition, further studies of bubble functions are used in mixed finite strain plasticity formulation with MINI element for quasi-incompressible plasticity fractures [54], and brittle and ductile models [14].

A bubble function supplements an additional displacement field at a node placed at centroid of triangle T. In contrast to the MINI element, ES-FEM constructs a displacement-based formulation. ES-FEM with a bubble function has only a linear displacement field as unknown which has value one at the centroid of triangle T and the pressure vanishes at the edges of triangle T. As shown in Fig. 3, and interior node is located at the geometric centre with an additional displacement field associated with the cube bubble.

The cubic bubble function introduced in [55] is used in this paper. Since the first three basis functions are not zero at the centroid $(1/3, 1/3)$, a basis function $\bar{\Psi}(\xi, \eta) = [1 - \xi - \eta, \ \xi, \ \eta, \ 27\xi\eta(1 - \xi - \eta)]^T$ is necessarily required transformation form gives as:

$$\Psi(\xi, \eta)^T = \bar{\Psi}(\xi, \eta)^T B_S^{-1} = [1 - \xi - \eta, \ \xi, \ \eta, \ 27\xi\eta(1 - \xi\eta)] \begin{bmatrix} 1 & 0 & 0 & 0 \\ 0 & 1 & 0 & 0 \\ 0 & 0 & 1 & 0 \\ -\frac{1}{3} & -\frac{1}{3} & -\frac{1}{3} & 1 \end{bmatrix} \tag{21}$$

and therefore the basis functions become as:

$$\Psi(\xi, \eta) = \begin{bmatrix} (1 - \xi - \eta) - 9\xi\eta(1 - \xi - \eta) \\ \xi - 9\xi\eta(1 - \xi - \eta) \\ \eta - 9\xi\eta(1 - \xi - \eta) \\ 27\xi\eta(1 - \xi - \eta) \end{bmatrix} \tag{22}$$

The properties of renewed basis functions and cubic bubble function of a right 45° three-node triangular element are given as (also see in Fig. 4):

$$\begin{cases} \Psi_b > 0 & \text{in } \Omega_e \\ \Psi_b = 0 & \text{on } \Gamma_e \\ \Psi_b = 1 & \text{at internal nodes} \end{cases} \tag{23}$$

4. Numerical examples

Three numerical examples, simple shear, lateral extension and "Not-so-simple" shear deformation, are chosen as benchmarks.[1] These examples are given in [46,48,56] with analytical solutions. Then, we test the behaviour of the method in the near-incompressible limit (Poisson's ratio $v \to 0.5$) for the Cook's membrane problem [57] with bulk moduli ($k = 1.96, 10, 10^2, 10^3, 10^4, 10^5, 10^6$ and 10^7) and mesh distortion sensitivity (artificially distorted meshes) for the problem of a block under bending [58].

4.1. Simple shear deformation

For simple shear deformation, the deformation gradient takes the form:

$$\mathbf{F} = \begin{bmatrix} 1 & k & 0 \\ 0 & 1 & 0 \\ 0 & 0 & 1 \end{bmatrix} \tag{24}$$

where $k > 0$. For this deformation, the strain invariants are:

$$I_1 = k^2 + 3 = I_2, \quad I_3 = 1 \tag{25}$$

Thus the incompressibility condition is always satisfied regardless of the material characteristics (isochoric deformation).

Substituting this in Eq. (2) gives the following strain energy function:

$$\mathcal{W} = \frac{\mu}{2}k^2 \tag{26}$$

---

[1] For these problems, following parameters for Newton-Raphson method are used: tolerance is 10^{-9}, the number of load step is 50–100 and the number of iteration to convergence is 4–6.
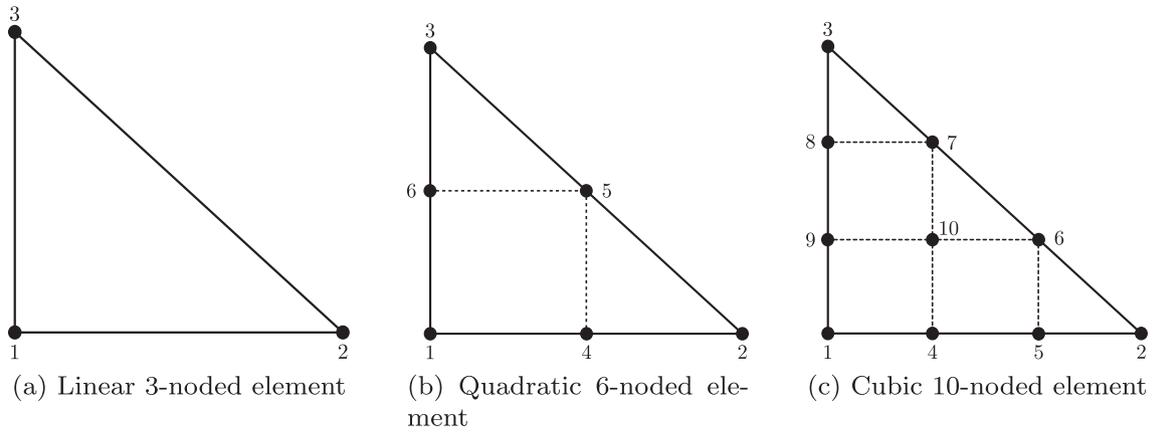
Fig. 3. Lagrange triangular elements: (a) linear Lagrange element, (b) quadratic Lagrange element and (c) cubic Lagrange element.

(a) Linear 3-noded element
(b) Quadratic 6-noded element
(c) Cubic 10-noded element
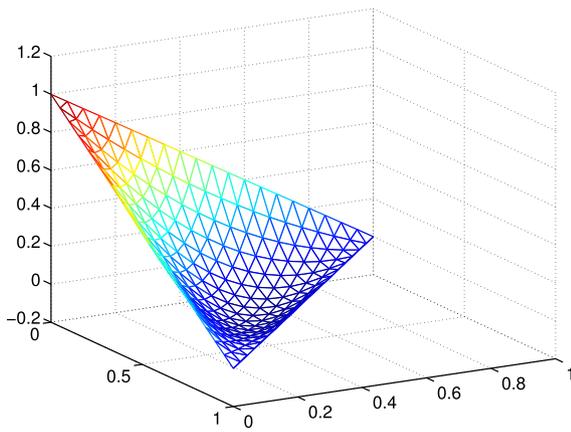
(a) Basis function Ψ_1
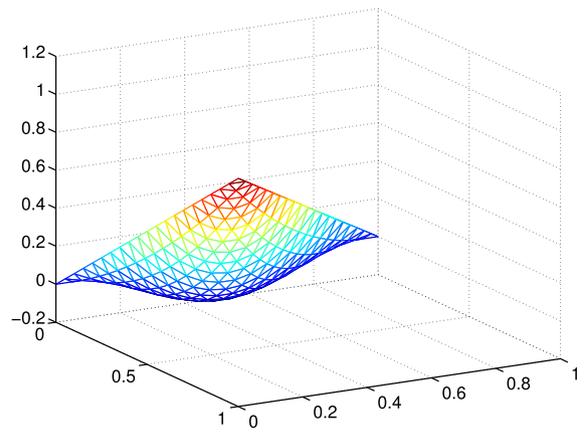
(b) Basis function Ψ_2
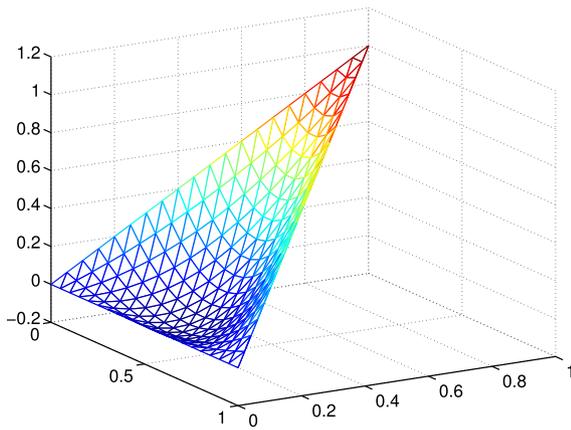
(c) Basis function Ψ_3
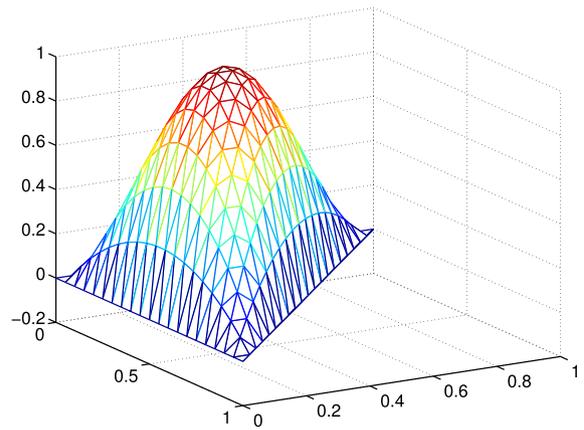
(d) Cubic bubble function Ψ_b

Fig. 4. Renewed basis functions and the cubic bubble function associated the centroid of a right 45° three-node triangular (T3) element.

The non-zero entries of the corresponding Cauchy stress tensor are [59,46]:

$$\sigma_{11} = \beta_0 + \beta_1(1 + k^2) + \beta_{-1},$$
$$\sigma_{22} = \beta_0 + \beta_1 + \beta_{-1}(1 + k^2),$$
$$\sigma_{33} = \beta_0 + \beta_1 + \beta_{-1},$$
$$\sigma_{12} = k(\beta_1 - \beta_{-1}),$$

(27)

where

$$\beta_0 = 2\frac{\partial \mathcal{W}}{\partial I_3} = -\mu, \quad \beta_1 = 2\frac{\partial \mathcal{W}}{\partial I_1} = \mu, \quad \beta_{-1} = 0. \tag{28}$$

Hence Eq. (27) can be written:

$$\sigma_{11} = k^2\mu, \quad \sigma_{22} = \sigma_{33} = 0, \quad \sigma_{12} = k\mu \tag{29}$$

The resulting first Piola-Kirchhoff stress tensor is then:

$$\mathbf{P} = \begin{bmatrix} \sigma_{11} - k\sigma_{12} & \sigma_{12} & 0 \\ \sigma_{12} - k\sigma_{22} & \sigma_{22} & 0 \\ 0 & 0 & \sigma_{33} \end{bmatrix} = \begin{bmatrix} 0 & k\mu & 0 \\ k\mu & 0 & 0 \\ 0 & 0 & 0 \end{bmatrix} \tag{30}$$

For this section, the shear and bulk moduli used are $\mu = 0.6$ and $\kappa = 100$, respectively. The higher value of κ, the material is more incompressible.

Dirichlet boundary conditions. To obtain the simple shear of a square section as shown in Fig. 5, the following Dirichlet boundary conditions can be imposed:

- All edges: $(u_1, u_2) = (kX_2, 0)$.

Fig. 6 illustrates the deformed shape of the standard FEM and the proposed technique for the simple shear deformation with Dirichlet boundary conditions when the deformation is $k = 1$ for both the FEM and the S-FEM.

The strain energies for the analytical, FEM and ES-FEM solutions are shown in Table 1. The analytical solution can be calculated by Eq. (26) and is such that $\mathcal{W} = 0.3$.

Table 1 provides the values of the relative error in strain energy for FEM, ES-FEM and NS-FEM. The values of the proposed formulations are within machine precision for moderate and coarse meshes.

4.2. Pure shear deformation

In this section pure shear deformation is considered, the deformation of pure shear is given as [46,60]:

$$x_1 = aX_1 + \sqrt{(b^2 - a^2)}X_2, \quad x_2 = bX_2, \quad x_3 = cX_3 \tag{31}$$

and therefore the deformation gradient for pure shear $\mathbf{F}$ is:

$$\mathbf{F} = \begin{bmatrix} a & \sqrt{b^2 - a^2} & 0 \\ 0 & b & 0 \\ 0 & 0 & 1 \end{bmatrix} \tag{32}$$

Therefore the left Cauchy-Green tensor $\mathbf{B}$ is:

$$\mathbf{B} = \mathbf{F}\mathbf{F}^\mathrm{T} = \begin{bmatrix} a & \sqrt{b^2 - a^2} & 0 \\ 0 & b & 0 \\ 0 & 0 & 1 \end{bmatrix} \begin{bmatrix} a & 0 & 0 \\ \sqrt{b^2 - a^2} & b & 0 \\ 0 & 0 & 1 \end{bmatrix}$$
$$= \begin{bmatrix} b^2 & b\sqrt{b^2 - a^2} & 0 \\ b\sqrt{b^2 - a^2} & b^2 & 0 \\ 0 & 0 & 1 \end{bmatrix} \tag{33}$$

The Cauchy stress is:

$$\boldsymbol{\sigma} = \begin{bmatrix} \mu(1 - b^2) & \mu b\sqrt{b^2 - a^2} & 0 \\ \mu b\sqrt{b^2 - a^2} & \mu(1 - b^2) & 0 \\ 0 & 0 & 0 \end{bmatrix} \tag{34}$$

Mixed boundary conditions. To obtain the pure shear of a square section, the mixed Neumann and Dirichlet boundary conditions can be imposed as follows:

- Bottom edge: $(P_1, u_2) = (-\sigma_{12}, 0)$;
- Left edge: $(P_1, P_2) = (\sigma_{11}, -\sigma_{21})$;
- Right edge: $(P_1, P_2) = (-\sigma_{11}, \sigma_{21})$;
- Top edge: $(P_1, P_2) = (\sigma_{12}, \sigma_{22})$.

The deformed shape of the approach for pure shear with the mixed Neumann and Dirichlet boundary conditions are shown in Fig. 7.

4.3. Uniform extension with lateral contraction

We deform a 3D sample of compressible material in Eq. (24) by the following triaxial stretch:

$$x_1 = \lambda_1 X_1, \quad x_2 = \lambda_2 X_2, \quad x_3 = \lambda_3 X_3 \tag{35}$$

where $\mathbf{X} = [X_1, X_2, X_3]^\mathrm{T}$ and $\mathbf{x} = [x_1, x_2, x_3]^\mathrm{T}$ denote the reference (Lagrangian) and current (Eulerian) coordinates, respectively, and $\lambda_i > 0$, $i = 1, 2, 3$, are positive constants. The corresponding deformation gradient is:

$$\mathbf{F} = \begin{bmatrix} \lambda_1 & 0 & 0 \\ 0 & \lambda_2 & 0 \\ 0 & 0 & \lambda_3 \end{bmatrix} \tag{36}$$

and the left Cauchy-Green tensor is $\mathbf{B} = \mathbf{F}\mathbf{F}^\mathrm{T}$.

We can then calculate the strain invariants using the following formulae:

$$I_1(\mathbf{B}) = \mathrm{tr}\mathbf{B}$$
$$I_2(\mathbf{B}) = \mathrm{tr}(\mathrm{cof}(\mathbf{B})) = \frac{1}{2}((\mathrm{tr}\mathbf{B})^2 - \mathrm{tr}\mathbf{B}^2) \tag{37}$$
$$I_3(\mathbf{B}) = \det\mathbf{B}$$

For the triaxial deformation, the strain invariants are:

$$I_1 = \lambda_1^2 + \lambda_2^2 + \lambda_3^2$$
$$I_2 = \lambda_1^2\lambda_2^2 + \lambda_2^2\lambda_3^2 + \lambda_3^2\lambda_1^2 \tag{38}$$
$$I_3 = \lambda_1^2\lambda_2^2\lambda_3^2$$

In particular, if the deformation is isochoric (preserves volume), then $I_3 = 1$.

The biaxial deformation associated with a square section of the material is then obtained by setting $\lambda_3 = 1$. In this case, if the deformation is isochoric, then $\lambda_2 = 1/\lambda_1$, and the strain invariants are:

$$I_1 = \lambda_1^2 + \frac{1}{\lambda_1^2} + 1 = I_2, \quad I_3 = 1 \tag{39}$$

Substituting these in Eq. (2) gives the following value for the strain energy function:
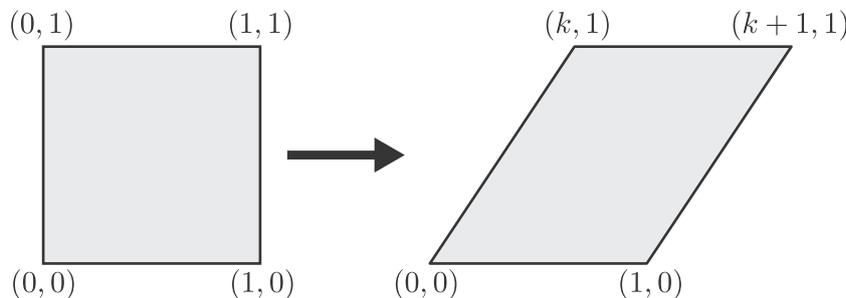

Fig. 5. Simple shear deformation of a unit square.
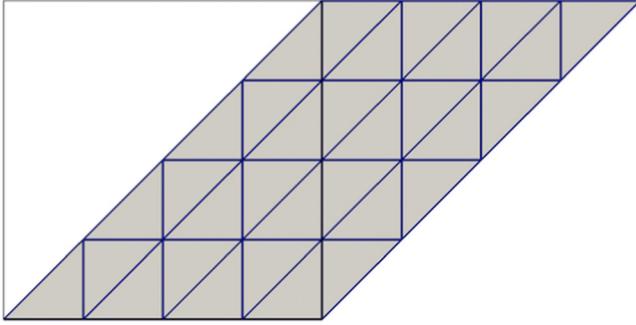
Fig. 6. Deformed shape for the simple shear deformation with Dirichlet BCs (4 × 4 T3 mesh with bulk modulus $\kappa = 100$).

Table 1
Strain energy relative error ($\times 10^{-12}$%) for the simple shear deformation with Dirichlet boundary conditions: FEM, edge-based smoothing and node-based-smoothing.

Num. of elements	FEM	ES-FEM	NS-FEM
4 × 4	0.0019	−0.0037	0.0056
8 × 8	−0.0019	0.0148	0.0037
16 × 16	0.0093	−0.0056	−0.0130
32 × 32	−0.0296	0.0500	0.0056

Strain energy relative error is given by: $\left(\frac{W_{\text{Numerical}} - W_{\text{Exact}}}{W_{\text{Exact}}}\right) \times 100\%$.
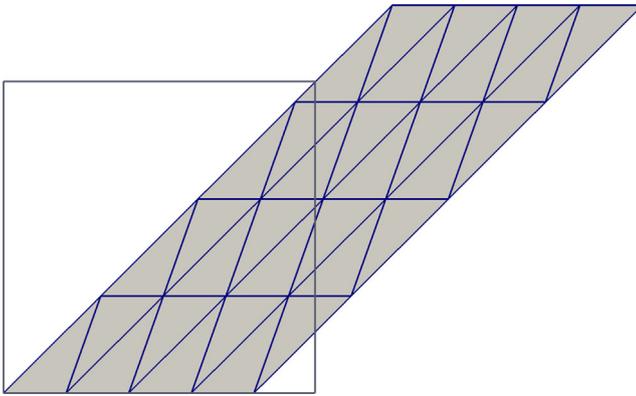

Fig. 7. Deformed shape for the pure shear deformation with Neumann BCs (4 × 4 T3 mesh with bulk modulus $\kappa = 100$).

$$\mathcal{W} = \frac{\mu}{2}\left(\lambda_1^2 + \frac{1}{\lambda_1^2} - 2\right) \tag{40}$$

By the Rivlin-Ericksen representation, the Cauchy stress takes the general form:

$$\boldsymbol{\sigma} = \beta_0 \mathbf{I} + \beta_1 \mathbf{B} + \beta_{-1} \mathbf{B}^{-1} \tag{41}$$

where the elastic response coefficients are calculated as follows:

$$\beta_0 = \frac{2}{\sqrt{I_3}}\left(I_2 \frac{\partial \mathcal{W}}{\partial I_2} + I_3 \frac{\partial \mathcal{W}}{\partial I_3}\right)$$
$$\beta_1 = \frac{2}{\sqrt{I_3}} \frac{\partial \mathcal{W}}{\partial I_1} \tag{42}$$
$$\beta_{-1} = -2\sqrt{I_3} \frac{\partial \mathcal{W}}{\partial I_2}$$

In particular, for the biaxial deformation of the square material, the non-zero components of the Cauchy stress are:

$$\sigma_{11} = \beta_0 + \beta_1 \lambda_1^2 + \beta_{-1}\frac{1}{\lambda_1^2}$$
$$\sigma_{22} = \beta_0 + \beta_1 \frac{1}{\lambda_1^2} + \beta_{-1}\lambda_1^2 \tag{43}$$
$$\sigma_{33} = \beta_0 + \beta_1 + \beta_{-1}$$

where

$$\beta_0 = 2\frac{\partial \mathcal{W}}{\partial I_3} = -\mu, \quad \beta_1 = 2\frac{\partial \mathcal{W}}{\partial I_1} = \mu, \quad \beta_{-1} = 0 \tag{44}$$

Hence, the non-zero components of the Cauchy stress tensor are:

$$\sigma_{11} = \mu(\lambda_1^2 - 1), \quad \sigma_{22} = \mu\left(\frac{1}{\lambda_1^2} - 1\right) \tag{45}$$

Dirichlet boundary conditions. To obtain the above biaxial stretch of a square section, assuming that the sides of the square are aligned with the directions X_1 and X_2, and the bottom left-hand corner is at the origin $O(0,0)$, then the following Dirichlet boundary conditions can be imposed:

- Bottom edge: $(u_1, u_2) = ((\lambda_1 - 1)X_1, 0)$;
- Left-hand edge: $(u_1, u_2) = (0, (1/\lambda_1 - 1)X_2)$;
- Top and right-hand edge: $(u_1, u_2) = ((\lambda_1 - 1)X_1, (1/\lambda_1 - 1)X_2)$.

The deformed shapes for the uniform extension with lateral contraction with Dirichlet boundary conditions are illustrated in Fig. 8. The relative strain energy errors are shown in Table 2.[2]

Mixed boundary conditions. Alternatively, Neumann boundary conditions can be imposed on some of the edges. Before we can do this, we need to recall the general formula for the first Piola-Kirchhoff stress tensor:

$$\mathbf{P} = \boldsymbol{\sigma}\text{cof}(\mathbf{F}) = \boldsymbol{\sigma}J\mathbf{F}^{-T} \tag{46}$$

Then, for the biaxial stretch with $\lambda_2 = 1/\lambda_1$ and $\lambda_3 = 1$, we obtain the following non-zero components for this tensor:

$$P_{11} = \frac{\sigma_{11}}{\lambda_1} = \mu\left(\lambda_1 - \frac{1}{\lambda_1}\right) = -P_{22} \tag{47}$$

At the corners, if one of the adjacent edges is subject to Dirichlet conditions and the other to Neumann conditions, the Dirichlet conditions are essential and take priority over the Neumann conditions. If both edges are subject to Neumann conditions, these are to be imposed simultaneously at the corner.

Fig. 9 represents the deformed shapes with mixed boundary conditions, and the relative errors for this problem are given in Table 3. Note that all methods provide, again, the exact results down to machine precision.

4.4. "Not-So-Simple" shear deformation

Consider now the non-homogeneous deformation:

$$x_1 = X_1 + kX_2^2, \quad x_2 = X_2, \quad x_3 = X_3 \tag{48}$$

for which the deformation gradient is:

$$\mathbf{F} = \begin{bmatrix} 1 & 2kX_2 & 0 \\ 0 & 1 & 0 \\ 0 & 0 & 1 \end{bmatrix} \tag{49}$$

where $k > 0$.

For clarity of presentation, denote $K = 2kX_2$. Then the strain invariants are:

---

[2] We observe that all methods provide the exact results at machine precision.
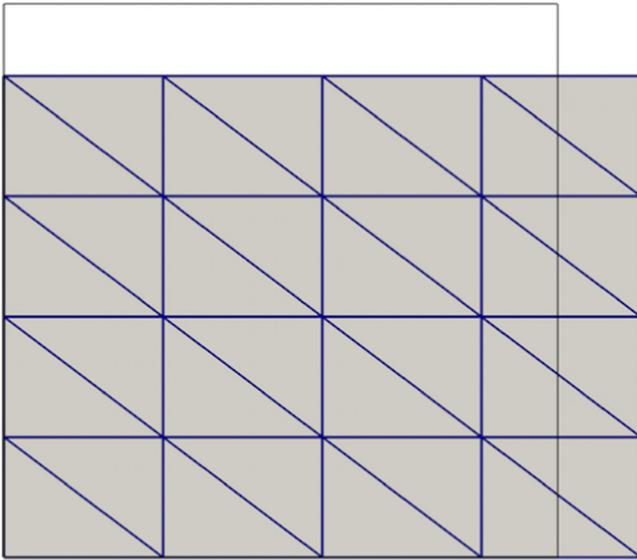
Fig. 8. Deformed shape for the uniform extension with lateral contraction with Dirichlet BCs (4×4 T3 mesh with bulk modulus $\kappa = 100$).

Table 2
Strain energy relative error ($\times 10^{-12}$%) for the uniform extension with lateral contraction with Dirichlet boundary conditions: FEM, edge-based smoothing and node-based smoothing.

Num. of elements	FEM	ES-FEM	NS-FEM
4×4	−0.0265	−0.0176	−0.0059
8×8	−0.0221	0.0132	−0.0103
16×16	−0.0882	−0.0147	−0.0471
32×32	0.3809	−0.3618	−0.0426

Strain energy relative error is given by: $\left(\frac{W_{\text{Numerical}} - W_{\text{Exact}}}{W_{\text{Exact}}} \right) \times 100\%$.
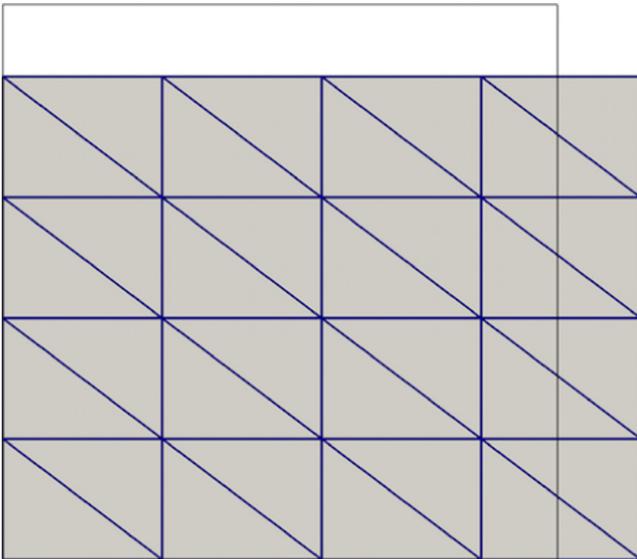
Fig. 9. Deformed shape for the uniform extension with lateral contraction with Neumann BCs (4×4 T3 mesh with the bulk modulus $\kappa = 100$).

$$I_1 = K^2 + 3 = I_2 \quad \text{and} \quad I_3 = 1 \tag{50}$$

and substituting Eq. (49) in Eq. (2) gives the strain energy function:

$$\mathcal{W} = \frac{\mu}{2} K^2 = \frac{\mu}{2} (2kX_2)^2 = 2\mu k^2 X_2^2 \tag{51}$$

Note that this function is not constant.

Table 3
Strain energy relative error ($\times 10^{-12}$%) for the uniform extension with lateral contraction with mixed Dirichlet and Neuman boundary conditions: FEM, edge-based smoothing and node-based smoothing.

Num. of elements	FEM	ES-FEM	NS-FEM
4×4	−0.0882	−0.0868	−0.0838
8×8	−0.0985	−0.0765	−0.0897
16×16	−0.1176	−0.1412	−0.1088
32×32	−0.0338	−0.4132	−0.1000

Strain energy relative error is given by: $\left(\frac{W_{\text{Numerical}} - W_{\text{Exact}}}{W_{\text{Exact}}} \right) \times 100\%$.

Dirichlet boundary conditions. To obtain the simple shear of a square section, the following Dirichlet boundary conditions can be imposed (see Fig. 10):

- All edges: $(u_1, u_2) = (kX_2^2, 0)$

The deformed shape of the "Not-so-simple" shear deformation is illustrated in Fig. 11. The strain energy relative errors for FEM and S-FEM are given in Table 4. The results of the FEM are comparable to those of the S-FEM; however, errors for ES-FEM and NS-FEM are globally small, around −0.4% and −0.5% respectively.

4.5. Near-incompressibility

In this section, near-incompressibility tests are studied. For these examples, different bulk moduli are used, $\kappa = 10^2$, 10^3 and 10^4. With those bulk moduli, for which the Poisson's ratio is close to 0.5, the model becomes nearly-incompressible. The geometry of the structure is illustrated in Fig. 12.

Fig. 13 represents the convergence of the strain energy for the standard FEM, ES-FEM, and NS-FEM with T3 elements. The numbers of elements along each side are 4×4, 8×8, 10×10, 16×16, 20×20, 32×32, 40×40 and 100×100. Because an analytical solution is not available for this problem we calculate a reference solution numerically using a mixed finite element method on a highly-refined mesh within the DOLFIN finite element software [61,62]. As shown in Fig. 13, edge- and node-based S-FEM are proven to be accurate and reliable for both compressible and nearly-incompressible problems. The x- and y-directions represent logarithmic number of global degrees of freedom and logarithm of a fraction of numerical results and analytical solution, respectively. When the Poisson's ratio is close to 0.5, the convergence of the ES-FEM becomes slow. The NS-FEM provides here an upper bound solution. Tables 5–7 provide the strain energy relative errors for FEM, ES-FEM and NS-FEM. As shown in Table 7, S-FEM handles near-incompressibility excellently, with results provided by NS-FEM up to 140 times more accurate than the FEM.

4.6. Mesh distortion sensitivity

In this section, a mesh distortion sensitivity is considered. For this test, results of DOLFIN finite element software are compared with the gradient smoothing techniques. We use artificially distorted meshes which are given by [35]:

$$\begin{aligned} x' &= x + r_c \alpha \triangle x \\ y' &= y + r_c \alpha \triangle y \end{aligned} \tag{52}$$

where r_c is a random number between −1.0 and 1.0, α is the magnitude of the distortion and $\triangle x$, $\triangle y$ are initial regular element sizes in the x- and y-direction. The higher α the more distorted the mesh.

The geometry of the examples is given in Sections 2.2.6 and 5.2.4 of [58] (see also Fig. 14). Consider a rectangle in the reference Cartesian coordinates (X, Y) defined by:
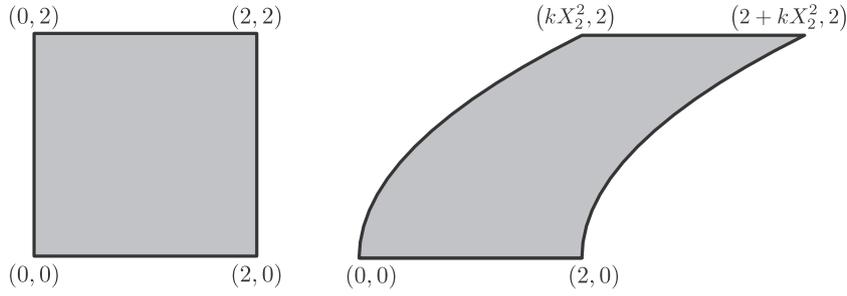
**Fig. 10.** "Not-So-Simple" shear deformation of a square.
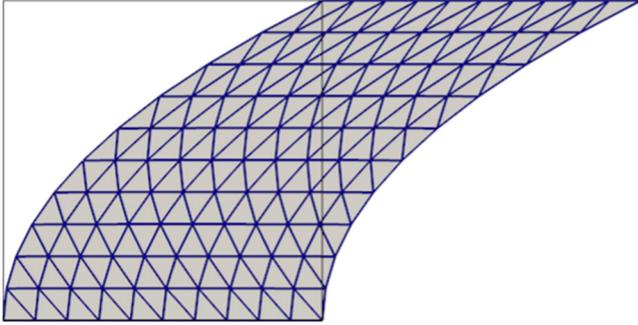
Fig. 11. Deformed shape for the "Not-So-Simple" shear deformation with Dirichlet BCs (10×10 T3 mesh with the bulk modulus $\kappa = 100$).

Table 4
Strain energy relative error (%) for the "Not-so-simple" shear example: edge-based and node-based smoothing.

Num. of elements	FEM	ES-FEM	NS-FEM
4×4	−1.7452	−2.9355	−5.2169
8×8	−0.6442	−1.0000	−1.6983
16×16	−0.3799	−0.4774	−0.6662
32×32	−0.3162	−0.3419	−0.3902

Strain energy relative error is given by: $\left(\frac{W_{\text{Numerical}} - W_{\text{Exact}}}{W_{\text{Exact}}} \right) \times 100\%$.
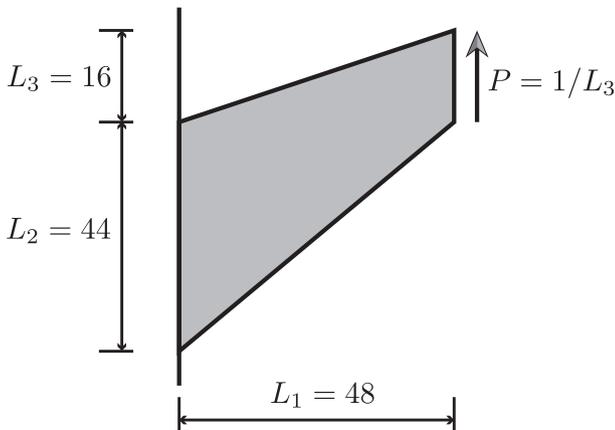

Fig. 12. The geometry of Cook's membrane with bending load.

$$X = (A_1, A_2), \quad Y = (-B, B), \quad Z = (0, 0) \tag{53}$$

where $(A_1, A_2, B > 0)$. The corresponding unit vector for current cylindrical coordinates (r, θ, z) are:

$$\mathbf{e}_r = \begin{bmatrix} \cos\theta \\ \sin\theta \\ 0 \end{bmatrix}, \quad \mathbf{e}_\theta = \begin{bmatrix} -\sin\theta \\ \cos\theta \\ 0 \end{bmatrix}, \quad \mathbf{e}_z = \begin{bmatrix} 0 \\ 0 \\ 0 \end{bmatrix} \tag{54}$$

The deformation in cylindrical coordinates is:

$$r = f(X) = \sqrt{2\alpha X}$$
$$\theta = g(Y) = \frac{1}{\alpha} Y \tag{55}$$
$$z = 0$$

For implementation, the given cylindrical coordinates are rewritten in Cartesian form:

$$x = r\cos\theta = \sqrt{2\alpha X} \cos\frac{Y}{\alpha}$$
$$y = r\sin\theta \sqrt{2\alpha X} \sin\frac{Y}{\alpha} \tag{56}$$
$$z = 0$$

Dirichlet boundary conditions. Dirichlet boundary conditions are imposed as following:

- Bottom edge ($Y = -B$):

$$u_x = \sqrt{2\alpha X} \cos\frac{-B}{\alpha} - X$$
$$u_y = \sqrt{2\alpha X} \sin\frac{-B}{\alpha} + B$$

- Top edge ($Y = B$):

$$u_x = \sqrt{2\alpha X} \cos\frac{B}{\alpha} - X$$
$$u_y = \sqrt{2\alpha X} \sin\frac{B}{\alpha} - B$$

- Left-hand edge ($X = A_1$):

$$u_x = \sqrt{2\alpha A_1} \cos\frac{Y}{\alpha} - A_1$$
$$u_y = \sqrt{2\alpha A_1} \sin\frac{Y}{\alpha} - Y$$

- Right-hand edge ($X = A_2$):

$$u_x = \sqrt{2\alpha A_2} \cos\frac{Y}{\alpha} - A_2$$
$$u_y = \sqrt{2\alpha A_2} \sin\frac{Y}{\alpha} - Y$$

Parameters, $\alpha = 0.9$, $A_1 = 2$, $A_2 = 3$ and $B = 2$ for Dirichlet boundary conditions, the distortion factors $\alpha = 0.1, 0.2, 0.3, 0.4$ and 0.45 for mesh distortion, and $\mu = 0.6$ and $\kappa = 1.95$ ($E \approx 1.6326$, $\nu \approx 0.3605$) for neo-Hookean material, are used in this test. In addition, we can obtain an exact solution for this example [58]. The deformation gradient $\mathbf{F}$ for this problem is:

$$\mathbf{F} = \begin{bmatrix} f' & 0 & 0 \\ 0 & fg' & 0 \\ 0 & 0 & 1 \end{bmatrix} \tag{57}$$

(a) $\kappa = 10^2$

(b) $\kappa = 10^3$

(c) $\kappa = 10^4$
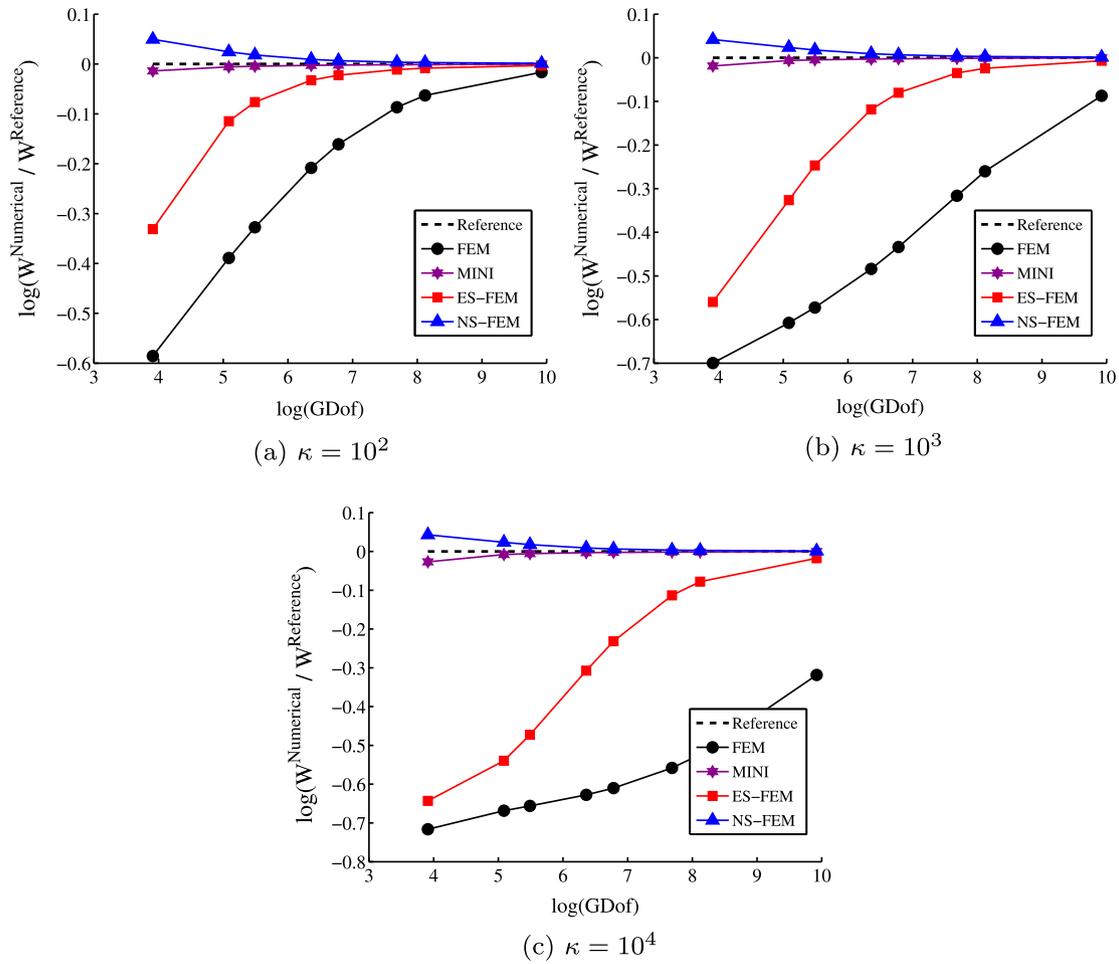
Fig. 13. Strain energy convergence of the Cook's membrane with the bulk moduli 10^2, 10^3 and 10^4: $W^{numerical}$ is numerical solutions of FEM and S-FEM, and $W^{References}$ is the solution of DOLFIN finite element software. For nearly-incompressible, S-FEM, particularly NS-FEM, performs much better than the classical FEM.

Table 5
Strain energies relative error of the Cook's membrane for the standard FEM, ES-FEM and NS-FEM with bulk modulus $\kappa = 100$.

	Bulk modulus $\kappa = 100$		
	FEM	ES-FEM	NS-FEM
4×4	−44.3239	−28.1828	5.0776
8×8	−32.2319	−10.8392	2.4749
16×16	−18.8038	−3.2010	0.9324
32×32	−8.3037	−1.1087	0.3672

Strain energy relative error is given by: $\left(\frac{W_{\text{Numerical}} - W_{\text{Exact}}}{W_{\text{Exact}}}\right) \times 100\%$.

Table 7
Strain energies relative error of the Cook's membrane for the standard FEM, ES-FEM and NS-FEM with bulk modulus $\kappa = 10,000$.

	Bulk modulus $\kappa = 10,000$		
	FEM	ES-FEM	NS-FEM
4×4	−51.1435	−47.4285	4.3948
8×8	−48.7502	−41.6966	2.3891
16×16	−46.6042	−26.4562	0.9102
32×32	−42.7694	−10.6931	0.3593

Strain energy relative error is given by: $\left(\frac{W_{\text{Numerical}} - W_{\text{Exact}}}{W_{\text{Exact}}}\right) \times 100\%$.

Table 6
Strain energies relative error of the Cook's membrane for the standard FEM, ES-FEM and NS-FEM with bulk modulus $\kappa = 1000$.

	Bulk modulus $\kappa = 1000$		
	FEM	ES-FEM	NS-FEM
4×4	−50.3251	−42.8593	4.2691
8×8	−45.5338	−27.8347	2.4078
16×16	−38.3660	−11.1631	0.9216
32×32	−27.1125	−3.4408	0.3649

Strain energy relative error is given by: $\left(\frac{W_{\text{Numerical}} - W_{\text{Exact}}}{W_{\text{Exact}}}\right) \times 100\%$.
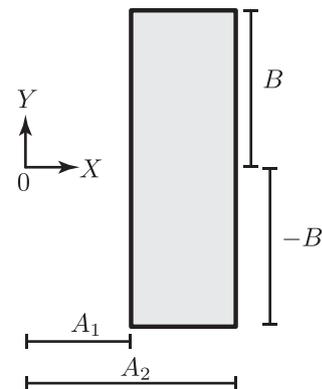

Fig. 14. The geometry of bending of a rectangle.

where f, g, f' and g' are:

$$f = \sqrt{2\alpha X}, \quad f' = \frac{\sqrt{2\alpha}}{2\sqrt{X}}, \quad g = \frac{1}{\alpha}Y, \quad g' = \frac{1}{\alpha} \tag{58}$$

The strain energy density can be rewritten as:

$$\mathcal{W} = \frac{1}{2}\mu(I_1 - 3) + \frac{1}{2}\lambda(\ln J)^2 - \mu \ln J = \frac{1}{2}\mu(I_1 - 3), \quad J = \sqrt{I_3} = 1 \tag{59}$$

where $I_1 = f^2 + (fg')^2 + 1$. Hence, Eq. (59) is:

$$\mathcal{W} = \frac{\mu}{2}\left(\frac{\alpha}{2X} + \frac{2X}{\alpha} - 2\right) = \mu \frac{(\alpha - 2X)^2}{4\alpha X} = \mu \frac{(0.9 - 2X)^2}{3.6X} \tag{60}$$

where $\alpha = 0.9$ and then strain energy is $W = \int_2^3 \int_{-2}^2 \mathcal{W}(X)dYdX \approx 4.485618$.

Fig. 15 illustrates the deformed configurations of bending block with different distortion factors. When the distortion factor α is close to 0.5, the meshes become severely distorted. In this test, we only impose Dirichlet boundary conditions which means that applied external forces vanish and no body force acts on the domain.

Detailed values of strain energy relative error are given in Tables 8–11. The relative error of S-FEM is much less than that of the FEM: errors for ES-FEM are about −1.0% and −1.9%, those of NS-FEM are around −1.5% and −3.5% with finer meshes (2 × 32 and 4 × 32) and highly distorted meshes (α = 0.45) whilst errors for FEM are approximately −0.7% and 260%. Moreover, MINI element gives accurate results; however, when meshes are severely distorted, MINI element fails to converge. This indicates that the S-FEM can effectively alleviate the mesh distortion sensitivity.

4.7. Edge-based smoothing strain using bubble functions

Lastly, we provide the results of the enhanced strain smoothing method, implementing Cook's membrane with the larger bulk moduli $\kappa = 10^5$, 10^6 and 10^7. Parameters which are used in this section are exactly the same as in the previous section. Fig. 16 illustrates the convergence of the strain energy. DOLFIN finite element software based on mixed finite element formulation on highly refined meshes is used as a reference solution.

The strain energy convergence of given techniques are described in Fig. 16. As shown in Fig. 16, NS-FEM performs much better than ES-FEM and the classical FEM. However the bubble-

(a) $\alpha = 0.0$ (b) $\alpha = 0.1$ (c) $\alpha = 0.2$
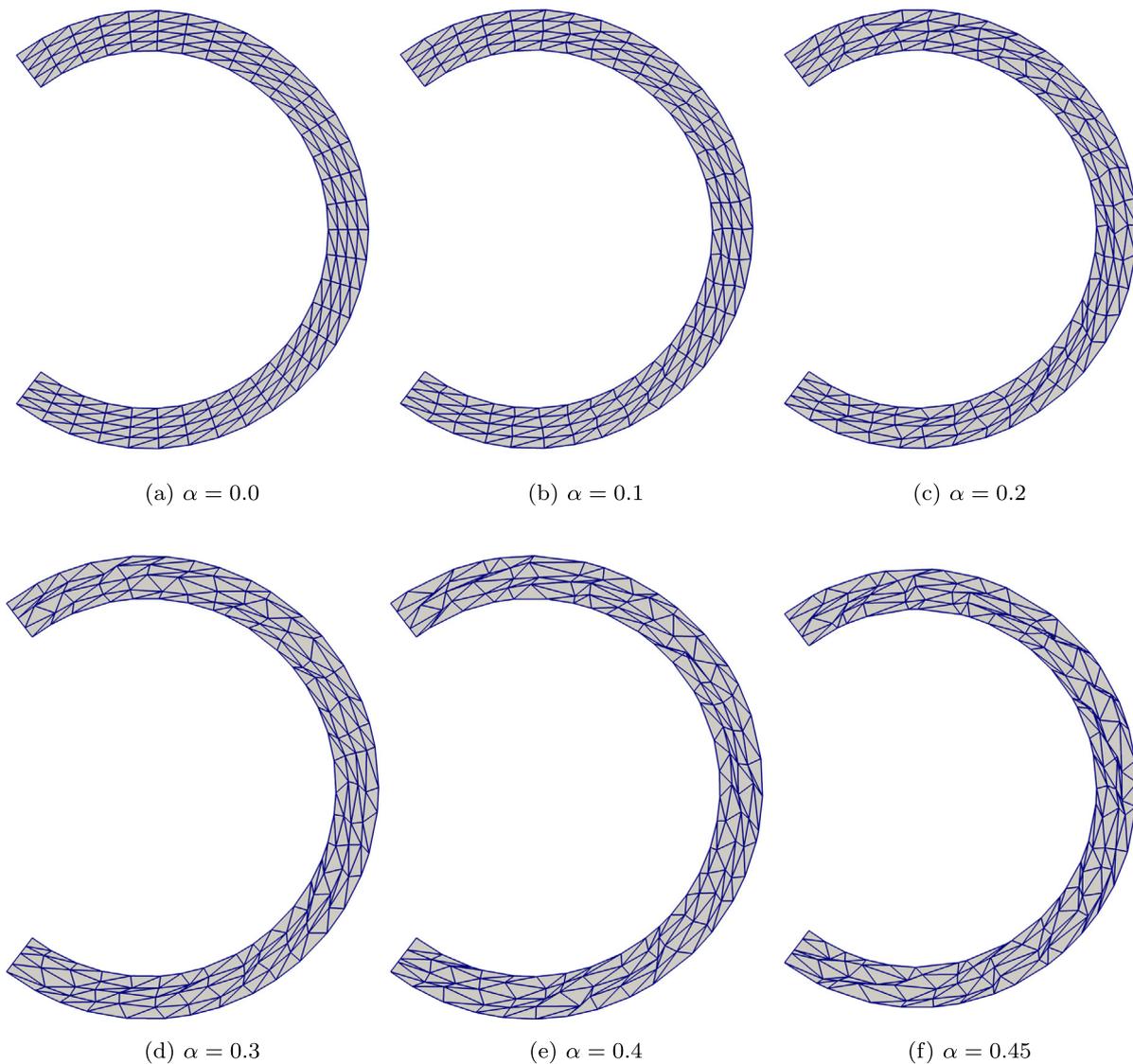
(d) $\alpha = 0.3$ (e) $\alpha = 0.4$ (f) $\alpha = 0.45$

Fig. 15. Deformed shape of the rectangle with different distortion factors: (a) regular mesh, (b) α = 0.1, (c) α = 0.2, (d) α = 0.3, (e) α = 0.4, (f) α = 0.45.

Table 8
Strain energies relative error for the bending of a rectangle using the standard FEM with α = 0.0, 0.1, 0.2, 0.3, 0.4 and 0.45. The higher the value of α the more distorted the mesh is.

	FEM					
	α = 0.0	α = 0.1	α = 0.2	α = 0.3	α = 0.4	α = 0.45
2×4	−0.0104	15.0394	207.8773	26.7563	372.4084	75.7918
2×8	−1.0311	−0.3799	2.9302	9.5888	16.1777	2.7048
2×16	−0.5370	−0.5493	−0.2529	1.0435	2.5121	−8.0411
2×32	−0.3738	−0.3704	−0.3814	−0.3209	−0.2496	−0.6437
4×4	−0.3003	20.9957	37.5691	98.2786	25.7889	415.3821
4×8	−1.3384	3.1601	6.9526	50.9083	5.8777	37.5263
4×16	−0.8566	−0.4581	0.6311	3.4588	0.5084	11.6704
4×32	−0.6992	−0.6773	−0.5890	−0.4389	−100.00	260.4544

Strain energy relative error is given by: $\left(\frac{W_{\text{Numerical}} - W_{\text{Exact}}}{W_{\text{Exact}}}\right) \times 100\%$.

Table 9
Strain energies relative error of bending of a rectangle for the ES-FEM with α = 0.0, 0.1, 0.2, 0.3, 0.4 and 0.45. The higher the value of α the more distorted the mesh is.

	ES-FEM					
	α = 0.0	α = 0.1	α = 0.2	α = 0.3	α = 0.4	α = 0.45
2×4	−10.2873	−5.2592	18.6808	4.2299	108.2842	99.6165
2×8	−4.7602	−4.6609	−3.2316	0.3819	3.3278	−3.1995
2×16	−1.8747	−1.8473	−1.7188	−1.4042	−1.0809	−0.6074
2×32	−1.0366	−1.0339	−1.0355	−1.0064	−1.0212	−0.9328
4×4	−10.4365	−1.6956	5.6167	38.2155	82.1832	398.7013
4×8	−4.8010	−2.6057	−0.7515	12.6831	18.5201	22.3123
4×16	−1.8911	−1.7469	−1.3835	−0.5151	−0.5468	−0.0267
4×32	−1.0479	−1.0406	−1.0317	−1.0076	−1.2111	−1.9604

Strain energy relative error is given by: $\left(\frac{W_{\text{Numerical}} - W_{\text{Exact}}}{W_{\text{Exact}}}\right) \times 100\%$.

Table 10
Strain energies relative error of bending of a rectangle for the NS-FEM with α = 0.0, 0.1, 0.2, 0.3, 0.4 and 0.45. The higher the value of α the more distorted the mesh is.

	NS-FEM					
	α = 0.0	α = 0.1	α = 0.2	α = 0.3	α = 0.4	α = 0.45
2×4	−18.7712	−16.8430	−15.2692	−16.6087	−17.5341	−33.9235
2×8	−8.9208	−9.1403	−9.3727	−8.2951	−6.9028	−5.3375
2×16	−3.4159	−3.4044	−3.4011	−3.4437	−3.5667	−1.2245
2×32	−1.7789	−1.7803	−1.7894	−1.7800	−1.8358	5.5170
4×4	−17.4487	−15.1659	−9.3829	−7.3456	−19.3577	7.1348
4×8	−8.6421	−8.4482	−8.4558	−8.1246	−8.7415	−7.7612
4×16	−3.1376	−3.1419	−3.1703	−3.1546	−3.1434	−3.6126
4×32	−1.4738	−1.4745	−1.4972	−1.5394	−2.0218	−3.5447

Strain energy relative error is given by: $\left(\frac{W_{\text{Numerical}} - W_{\text{Exact}}}{W_{\text{Exact}}}\right) \times 100\%$.

Table 11
Strain energies relative error of bending of a rectangle for the MINI element with α = 0.0, 0.1, 0.2, 0.3, 0.4 and 0.45. The higher the value of α the more distorted the mesh is.

	MINI					
	α = 0.0	α = 0.1	α = 0.2	α = 0.3	α = 0.4	α = 0.45
2×4	0.04954	8.7773	139.3670	21.8627	DNC*	DNC*
2×8	−1.1833	−0.8831	0.7415	5.3501	9.2233	0.4476
2×16	−0.6882	−0.7193	−0.5462	0.1692	0.9047	0.3323
2×32	−0.4992	−0.4984	−0.5096	−0.4703	−0.4430	−0.4142
4×4	−0.1426	13.8506	28.6429	83.3968	112.1389	DNC*
4×8	−1.3670	1.5785	3.7108	37.2203	35.9437	53.4136
4×16	−0.8857	−0.7011	−0.1721	1.2907	0.9638	2.7327
4×32	−0.7181	−0.7094	−0.6777	−0.6245	−0.8825	−1.6318

Strain energy relative error is given by: $\left(\frac{W_{\text{Numerical}} - W_{\text{Exact}}}{W_{\text{Exact}}}\right) \times 100\%$.
DNC*: Did Not Converge.

enhanced ES-FEM produces more accurate results and higher convergence rates than NS-FEM. It is clearly shown that the bubble function within ES-FEM effectively improves the quality of T3 elements in the nearly-incompressible limit.

Relative errors in the strain energy for FEM, ES-FEM, NS-FEM and ES-FEM with the bubbles are given in Tables 12–15. The relative errors of FEM and ES-FEM are around 50% for both methods with fine meshes, whereas NS-FEM and bES-FEM prevent volumet-

(a) $\kappa = 10^5$

(b) $\kappa = 10^6$

(c) $\kappa = 10^7$
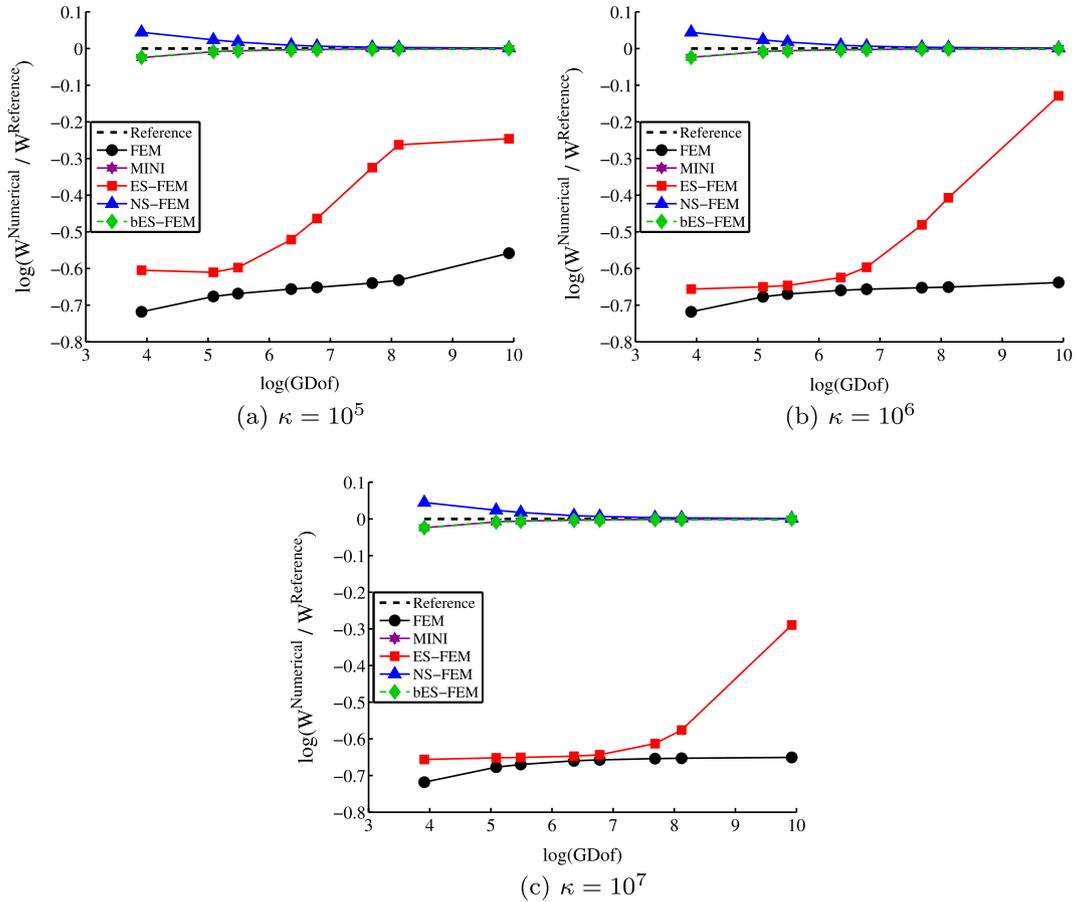
Fig. 16. Strain energy convergence of the Cook's membrane with the bulk moduli $\kappa = 10^5$, 10^6 and 10^7: DOLFIN finite element software is to be the reference solution.

Table 12
Strain energies relative error of the Cook's membrane for the standard FEM with bulk moduli $\kappa = 10^5$, 10^6 and 10^7.

	FEM		
	$\kappa = 10^5$	$\kappa = 10^6$	$\kappa = 10^7$
4×4	−51.2286	−51.2284	−51.2380
8×8	−49.1550	−49.1967	−49.2009
16×16	−48.1180	−48.2921	−48.3098
32×32	−47.2637	−47.9235	−47.9486

Strain energy relative error is given by: $\left(\frac{W_{\text{Numerical}} - W_{\text{Reference}}}{W_{\text{Reference}}}\right) \times 100\%$.

Table 13
Strain energies relative error of the Cook's membrane for the standard ES-FEM with bulk moduli $\kappa = 10^5$, 10^6 and 10^7.

	ES-FEM		
	$\kappa = 10^5$	$\kappa = 10^6$	$\kappa = 10^7$
4×4	−45.3871	−48.1101	−48.1194
8×8	−45.6787	−47.7943	−47.8887
16×16	−40.6140	−46.4490	−47.6438
32×32	−27.7231	−38.1638	−45.8184

Strain energy relative error is given by: $\left(\frac{W_{\text{Numerical}} - W_{\text{Reference}}}{W_{\text{Reference}}}\right) \times 100\%$.

Table 14
Strain energies relative error of the Cook's membrane for the standard NS-FEM with the higher bulk moduli $\kappa = 10^5$, 10^6 and 10^7.

	NS-FEM		
	$\kappa = 10^5$	$\kappa = 10^6$	$\kappa = 10^7$
4×4	4.5274	4.5461	4.5756
8×8	2.3875	2.4000	2.3907
16×16	0.9097	0.9113	0.9130
32×32	0.3576	0.3594	0.3593

Strain energy relative error is given by: $\left(\frac{W_{\text{Numerical}} - W_{\text{Reference}}}{W_{\text{Reference}}}\right) \times 100\%$.

Table 15
Strain energies relative error of the Cook's membrane for the standard ES-FEM with the bubbles with bulk moduli $\kappa = 10^5$, 10^6 and 10^7.

	bES-FEM		
	$\kappa = 10^5$	$\kappa = 10^6$	$\kappa = 10^7$
4×4	−2.3551	−2.3552	−2.3552
8×8	−0.8061	−0.8061	−0.8061
16×16	−0.3952	−0.3952	−0.3952
32×32	−0.2010	−0.2010	−0.2010

Strain energy relative error is given by: $\left(\frac{W_{\text{Numerical}} - W_{\text{Reference}}}{W_{\text{Reference}}}\right) \times 100\%$.

ric locking in quasi-incompressible limit $(\nu \to 0.5)$. Notable improvement of the bubble-enhanced ES-FEM is that its relative errors, −0.8% for the bulk moduli $\kappa = 10^5$, 10^6 and 10^7 with 8×8 elements, are smaller than those of NS-FEM, 0.9% for the bulk mod-

uli $\kappa = 10^5$, 10^6 and 10^7 with 16×16 elements. In other words, bubble-enriched ES-FEM has more accurate results and faster convergence and overcomes the overestimation of the stiffness matrix and the locking problems.

5. Conclusions

In this work, we reviewed the basic theory of the smoothed finite element method in linear and finite elasticity. Through numerical examples, we showed the accuracy and convergence of the proposed method in hyperelasticity, and its ability to overcome locking and mesh distortion effects.

We also presented the analytical solutions for Simple Shear deformation with Dirichlet boundary conditions, Uniform Extension with lateral contraction with both Dirichlet and mixed boundary conditions, and "Not-So-Simple" Shear deformation with Dirichlet boundary conditions. We analysed the accuracy of the proposed technique, compared to those analytical solutions and numerical results obtained with FEM.

To show the ability of the method to handle nearly-incompressible problems, bulk moduli $\kappa = 1.95$, 10, 10^2, 10^3 and 10^4 were used. For nearly-incompressible problems, FEM provides very slow convergence, whereas S-FEM is shown to be stable and accurate. When the bulk modulus is large, ES-FEM reveals relatively slower convergence than NS-FEM. Although NS-FEM itself is stable and reliable for near-incompressibility, enhanced ES-FEM, using the bubble functions, sufficiently improves the quality of lower-order simplex element and prevents the locking issue under large deformations.

Lastly, to study mesh distortion sensitivity, artificially distorted meshes are constructed with various distortion factors. For heavily distorted meshes, FEM shows unreliable results, whilst S-FEM performs very well.

As shown in the numerical examples the S-FEM is able to alleviate the spurious effects of both shear locking and mesh distortion whilst requiring only simplex elements, meshes of which are easily generated. It is therefore apparent that these elements, which are easily implemented within existing FE codes offer an alternative to quadrilateral elements. We are currently extending this work to 3D hyperelastic problems and proceeding to GPU implementation for real-time applications [63].

Appendix A. Smoothed deformation gradient

If the deformation gradient $\mathbf{F}$ is homogeneous on element, the displacement field on a single element can be explained as follows:

$$\mathbf{u}(\mathbf{X}) = \begin{bmatrix} u_1(\mathbf{X}) \\ u_2(\mathbf{X}) \end{bmatrix} = \begin{bmatrix} a_{11}X_1 + a_{12}X_2 + b_1 \\ a_{21}X_1 + a_{22}X_2 + b_2 \end{bmatrix} \tag{A.1}$$

where the undetermined coefficients a_{ij} and b_i, for $i, j = 1, 2$, are constant.

We here consider the smoothed deformation gradient $\tilde{\mathbf{F}}$ for ES-FEM. The deformation gradient on a triangle $\triangle ABC$ for the standard FEM in Fig. A1 is:

$$\mathbf{F} = \begin{bmatrix} a_{11}+1 & a_{12} \\ a_{21} & a_{22}+1 \end{bmatrix} = \begin{bmatrix} (u_1^B - u_1^A)/h + 1 & (u_1^C - u_1^A)/h \\ (u_2^B - u_2^A)/h & (u_2^C - u_2^A)/h + 1 \end{bmatrix}$$

For the smoothed deformation gradient $\tilde{\mathbf{F}}$ in the smoothing domain Ω_k in Fig. A.1, the deformation gradient in the smoothing domain Ω_k^1 can be expressed as following:

$$u_1(O_1) = \frac{1}{3}(u_1^A + u_1^B + u_1^C), \quad u_2(O_1) = \frac{1}{3}(u_2^A + u_2^B + u_2^C) \tag{A.2}$$

Substituting Eq. (A.2) into Eq. (A.1), the displacement field on mid-point O_1 is given by:

$$\frac{1}{3}(u_1^A + u_1^B + u_1^C) = a_{11}\frac{h}{3} + a_{12}\frac{h}{3} + b_1$$

$$\frac{1}{3}(u_2^A + u_2^B + u_2^C) = a_{21}\frac{h}{3} + a_{22}\frac{h}{3} + b_2$$

Similarly, the displacement fields on node B and C can be written as:

$$u_1^B = a_{11}h + b_1, \quad u_2^B = a_{21}h + b_2 \tag{A.3}$$

and
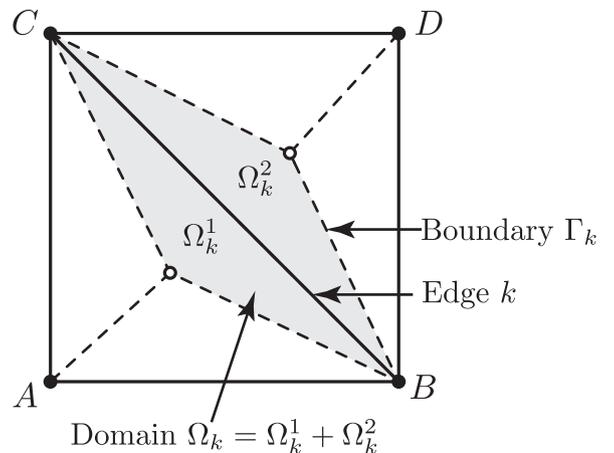
(a) Smoothing domain associated with target edge k in ES-FEM
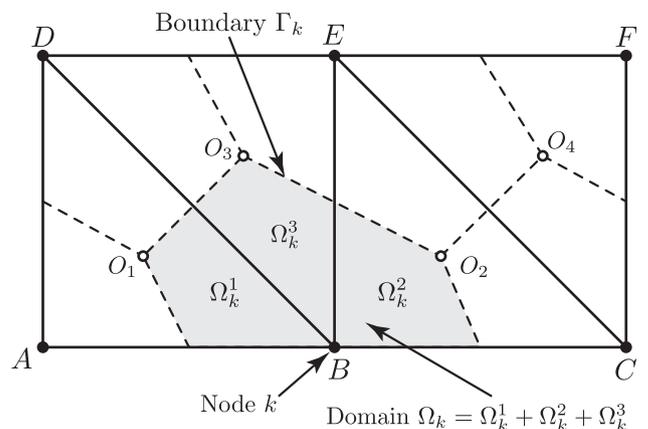
(b) Smoothing domain associated with target node k in NS-FEM

Fig. A.1. Smoothing domains associated target edge k for ES-FEM and node k for NS-FEM to assemble the smoothed deformation gradient $\tilde{\mathbf{F}}$.

$$u_1^C = a_{12}h + b_1, \quad u_2^C = a_{22}h + b_2 \tag{A.4}$$

Substituting Eq. (A.4) into Eq. (A.3), we obtain:

$$a_{11} - a_{12} = \frac{u_1^B - u_1^C}{h}, \quad a_{21} - a_{22} = \frac{u_2^B - u_2^C}{h}$$

Hence, the displacements on the mid-point O_1 are given by:

$$\begin{aligned} u_1^A + u_1^B + u_1^C &= a_{11}h + a_{12}h + 3(u_1^C - a_{12}h) \\ u_2^A + u_2^B + u_2^C &= a_{21}h + a_{22}h + 3(u_2^C - a_{22}h) \end{aligned} \tag{A.5}$$

From Eq. (A.5), the undetermined coefficient a_{ij} are defined as follows:

$$a_{11} = \frac{u_1^B - u_1^A}{h}, \quad a_{12} = \frac{u_1^C - u_1^A}{h}, \quad a_{21} = \frac{u_2^B - u_2^A}{h}, \quad a_{22} = \frac{u_2^C - u_2^A}{h}$$

Similarly, the undetermined coefficient a_{ij} for triangle $\triangle DCB$ in Fig. A.1 are given by:

$$a_{11} = \frac{u_1^C - u_1^D}{h}, \quad a_{12} = \frac{u_1^B - u_1^D}{h}, \quad a_{21} = \frac{u_2^C - u_2^D}{h}, \quad a_{22} = \frac{u_2^B - u_2^D}{h}$$

The smoothed deformation gradient is given by Hu et al. [64]:

$$\tilde{F}_{ij}(\mathbf{x}_k) = \frac{1}{A_k} \int_{\Omega_k} F_{ij}(\mathbf{x}) \Phi(\mathbf{x}) \mathrm{d}\Omega = \frac{1}{A_k} \int_{\Omega_k} \left(\frac{\partial u_i^h}{\partial X_j} \right) \Phi(\mathbf{x}) \mathrm{d}\Omega + \delta_{ij}$$

where Φ is:

$$\Phi = \begin{cases} 1 & \mathbf{x} \in \Omega_k \\ 0 & \text{otherwise} \end{cases} \tag{A.6}$$

and then:

$$\tilde{F}_{11} = \frac{1}{A_k} \left\{ \int_{\Omega_k^1} \frac{\partial u_1^h}{\partial X_1} \mathrm{d}\Omega + \int_{\Omega_k^2} \frac{\partial u_1^h}{\partial X_1} \mathrm{d}\Omega \right\} + 1 = \frac{3}{h^2} \left(a_{11}^1 \frac{h^2}{6} + a_{11}^2 \frac{h^2}{6} \right) + 1$$

$$\tilde{F}_{12} = \frac{1}{A_k} \left\{ \int_{\Omega_k^1} \frac{\partial u_1^h}{\partial X_2} \mathrm{d}\Omega + \int_{\Omega_k^2} \frac{\partial u_1^h}{\partial X_2} \mathrm{d}\Omega \right\} = \frac{3}{h^2} \left(a_{12}^1 \frac{h^2}{6} + a_{12}^2 \frac{h^2}{6} \right)$$

$$\tilde{F}_{21} = \frac{1}{A_k} \left\{ \int_{\Omega_k^1} \frac{\partial u_2^h}{\partial X_1} \mathrm{d}\Omega + \int_{\Omega_k^2} \frac{\partial u_2^h}{\partial X_1} \mathrm{d}\Omega \right\} = \frac{3}{h^2} \left(a_{21}^1 \frac{h^2}{6} + a_{21}^2 \frac{h^2}{6} \right)$$

$$\tilde{F}_{22} = \frac{1}{A_k} \left\{ \int_{\Omega_k^1} \frac{\partial u_2^h}{\partial X_2} \mathrm{d}\Omega + \int_{\Omega_k^2} \frac{\partial u_2^h}{\partial X_2} \mathrm{d}\Omega \right\} + 1 = \frac{3}{h^2} \left(a_{22}^1 \frac{h^2}{6} + a_{22}^2 \frac{h^2}{6} \right) + 1$$

where $A_k = A_k^1 + A_k^2 = \frac{h^2}{6} + \frac{h^2}{6} = \frac{h^2}{3}$, and the matrix form is:

$$\tilde{\mathbf{F}} = \begin{bmatrix} \frac{1}{2} \left(\frac{u_1^B - u_1^A}{h} + \frac{u_1^C - u_1^D}{h} \right) + 1 & \frac{1}{2} \left(\frac{u_1^C - u_1^A}{h} + \frac{u_1^B - u_1^D}{h} \right) \\ \frac{1}{2} \left(\frac{u_2^B - u_2^A}{h} + \frac{u_2^C - u_2^D}{h} \right) & \frac{1}{2} \left(\frac{u_2^C - u_2^A}{h} + \frac{u_2^B - u_2^D}{h} \right) + 1 \end{bmatrix} \tag{A.7}$$

In case the edge is on the boundary, the smoothed deformation gradient $\tilde{\mathbf{F}}$ can be described as following:

$$\tilde{\mathbf{F}} = \begin{bmatrix} \frac{1}{2} \left(\frac{u_1^B - u_1^A}{h} \right) + 1 & \frac{1}{2} \left(\frac{u_1^C - u_1^A}{h} \right) \\ \frac{1}{2} \left(\frac{u_2^B - u_2^A}{h} \right) & \frac{1}{2} \left(\frac{u_2^C - u_2^A}{h} \right) + 1 \end{bmatrix} \tag{A.8}$$

References

[1] Bommes D, Lévy B, Pietroni N, Puppo E, Silva C, Tarini M, et al. Quad-mesh generation and progressing: a survey. Comput Graph Forum 2013;32(6):51–76.
[2] Bonet J, Burton A. A simple average nodal pressure tetrahedral element for incompressible and nearly incompressible dynamic explicit applications. Commun Numer Methods Eng 1998;14(5):437–49.
[3] Joldes G, Wittek A, Miller K. Non-locking tetrahedral finite element for surgical simulation. Commun Numer Methods Eng 2009;25(7):827–36.
[4] Bonet J, Marriott H, Hassan O. Stability and comparison of different linear tetrahedral formulations for nearly incompressible explicit dynamic applications. Int J Numer Methods Eng 2001;50:119–33.
[5] Belytschko T, Krongauz Y, Organ D, Fleming M, Krysl P. Meshless methods: an overview and recent developments. Comput Methods Appl Mech Eng 1996;139(1–4):3–47.
[6] Liu G. Meshfree methods: moving beyond and the finite element method. CRC Press; 2003.
[7] Liu G, Gu Y. An introduction to meshfree methods and their programming. Springer; 2005.
[8] Huerta A, Vidal Y, Villon P. Pseudo-divergence-free element free Galerkin method for incompressible fluid flow. Comput Methods Appl Mech Eng 2004;193(12–14):1119–36.
[9] Rabczuk T, Areias P, Belytschko T. A simplified meshfree method for shear bands with cohesive surfaces. Int J Numer Methods Eng 2007;69(5):993–1021.
[10] Rabczuk T, Samaniego E. Discontinuous modelling of shear bands using adaptive meshfree methods. Comput Methods Appl Mech Eng 2008;197(6–8):641–58.
[11] Mathisen K, Okstad K, Kvamsdal T, Raknes S. Isogeometric analysis of finite deformation nearly incompressible solids. J Struct Mech 2011;44(3):260–78.
[12] Taylor R. Isogeometric analysis of nearly incompressible solids. Int J Numer Methods Eng 2011;87(1–5):273–88.
[13] Areias P, Rabczuk T. Finite strain fracture of plates and shells with configurational forces and edge rotation. Int J Numer Methods Eng 2013;94(12):1099–122.
[14] Areias P, Rabczuk T, Camanho P. Finite strain fracture of 2D problems with injected anisotropic softening elements. Theoret Appl Fract Mech 2014;72:50–63.
[15] Simo J, Taylor R, Pister K. Variational and projection methods for the volume constraint in finite deformation elasto-plasticity. Comput Methods Appl Mech Eng 1985;51:177–208.
[16] Simo J, Rifai M. A class of mixed assumed strain methods and the method of incompatible modes. Int J Numer Methods Eng 1990;29(8):1595–638.
[17] Chiumenti M, Valverde Q, Agelet de Saracibar C, Cervera M. A stabilized formulation for incompressible elasticity using linear displacement and pressure interpolations. Comput Methods Appl Mech Eng 2002;191(46):5253–64.
[18] Liu G, Dai K, Nguyen T. A smoothed finite element method for mechanics problems. Comput Mech 2007;39(6):859–77.
[19] Liu G, Nguyen T, Dai K, Lam K. Theoretical aspects of the smoothed finite element method (SFEM). Int J Numer Methods Eng 2007;71(8):902–30.
[20] Chen J-S, Wu C-T, Yoon S, You Y. A stabilized conforming nodal integration for Galerkin mesh-free methods. Int J Numer Methods Eng 2001;50(2):435–66.
[21] Chen J-S, Yoon S, Wu C-T. Non-linear version of stabilized conforming nodal integration for Galerkin mesh-free methods. Int J Numer Methods Eng 2002;53(12):2587–615.
[22] Yoo J, Moran B, Chen J-S. Stabilized conforming nodal integration in the natural-element method. Int J Numer Methods Eng 2004;60(5):861–90.
[23] Natarajan S, Bordas S, Roy Mahapatra D. Numerical integration over arbitrary polygonal domains based on Schwarz-Christoffel conformal mapping. Int J Numer Methods Eng 2009;80(1):103–34.
[24] Natarajan S, Mahapatra D, Bordas S. Integrating strong and weak discontinuities without integration subcells and examples applications in an XFEM/GFEM framework. Int J Numer Methods Eng 2010;83(3):269–94.
[25] Zhang H, Liu S, Li L. On the smoothed finite element method. Int J Numer Methods Eng 2008;77(13):1285–95.
[26] Le C, Nguyen-Xuan H, Askes H, Bordas S, Rabczuk T, Nguyen-Vinh H. A cell-based smoothed finite element method for kinematic limit analysis. Int J Numer Methods Eng 2010;83(12):1651–74.
[27] Liu G, Nguyen-Thoi T, Nguyen-Xuan H, Dai K, Lam K. On the essence and the evaluation of the shape functions for the smoothed finite element method (SFEM). Int J Numer Methods Eng 2009;77(13):1863–9.
[28] Liu G, Nguyen-Xuan H, Nguyen-Thoi T. A theoretical study on the smoothed FEM (S-FEM) models: properties, accuracy and convergence rates. Int J Numer Methods Eng 2010;84(10):1222–56.
[29] Bordas S, Natarajan S. On the approximation in the smoothed finite element method (SFEM). Int J Numer Methods Eng 2010;81(5):660–70.
[30] Dai K, Liu G, Nguyen T. An n-sided polygonal smoothed finite element method (nSFEM) for solid mechanics. Finite Elem Anal Des 2007;43(11–12):847–60.
[31] Nguyen-Xuan H, Rabczuk T, Bordas S, Debongnie J. A smoothed finite element method for plate analysis. Comput Methods Appl Mech Eng 2008;197(13–16):1184–203.
[32] Cui X, Liu G, Li G, Zhao X, Nguyen T, Sun G. A smoothed finite element method (SFEM) for linear and geometrically nonlinear analysis of plates and shells. Comput Model Eng Sci 2008;28(2):109–25.
[33] Nguyen-Xuan H, Liu G, Thai-Hoang C, Nguyen-Thoi T. An edge-based smoothed finite element method (ES-FEM) with stabilized discrete shear gap technique for analysis of Reissner-Mindlin plates. Comput Methods Appl Mech Eng 2010;199(9–12):471–89.
[34] Wu C, Wang H. An enhanced cell-based smoothed finite element method for the analysis of Reissner-Mindlin plate bending problems involving distorted mesh. Int J Numer Methods Eng 2013;95(4):288–312.
[35] Bordas S, Rabczuk T, Nguyen-Xuan H, Nguyen VP, Natarajan S, Bog T, et al. Strain smoothing in FEM and XFEM. Comput Struct 2010;88(23–24):1419–43.
[36] Nguyen-Xuan H, Liu G. An edge-based smoothed finite element method softened with a bubble function (bES-FEM) for solid mechanics problems. Comput Struct 2013;128:14–30.
[37] Liu G, Nguyen-Thoi T, Nguyen-Xuan H, Lam K. A node-based smoothed finite element method (NS-FEM) for upper bound solutions to solid mechanics problems. Comput Struct 2009;87(1–2):14–26.

[38] Liu G, Nguyen T. Smoothed finite element methods. CRC Press; 2010.
[39] Nguyen T, Liu G, Dai K, Lam K. Selective smoothed finite element method. Tsinghua Sci Technol 2007;12(5):497–508.
[40] Liu G, Zhang G. Upper bound solution to elasticity problems: a unique property of the linear conforming point interpolation method (LC-PIM). Int J Numer Methods Eng 2008;74(7):1128–61.
[41] Nguyen-Thanh N, Rabczuk T, Nguyen-Xuan H, Bordas S. An alternative alpha finite element method (AαFEM) for free and forced structural vibration using triangular meshes. J Comput Appl Math 2010;233(9):2112–35.
[42] Liu G, Nguyen-Thoi T, Lam K. An edge-based smoothed finite element method (ES-FEM) for static, free and forced vibration analyses of solids. J Sound Vib 2009;320(4–5):1100–30.
[43] Zhang Z-Q, Liu G. Temporal stabilization of the node-based smoothed finite element method and solution bound of linear elastostatics and vibration problems. Comput Mech 2010;46(2):229–46.
[44] Zhang Z-Q, Liu G. Upper and lower bounds for natural frequencies: a property of the smoothed finite element method. Int J Numer Methods Eng 2010;84(2):149–78.
[45] Dai K, Liu G. Free and forced vibration analysis using the smoothed finite element method (SFEM). J Sound Vib 2007;301(3–5):803–20.
[46] Angela Mihai L, Goriely A. Numerical simulation of shear and the Poynt-ing effects by the finite element method: an application of the generalised empirical inequalities in non-linear elasticity. Int J Non-Linear Mech 2013;49:1202–11.
[47] Le Tallec P. Numerical methods for three-dimensional elasticity. In: Ciarlet P, Lions J, editors. Handbook of numerical analysis, vol. III. North-Holland; 1994. p. 465–624.
[48] Oden J. Finite elements of nonlinear continua. Dover; 2006.
[49] Belytschko T, Moran B, Liu W. Nonlinear finite element analysis for continua and structures. Wiley; 1999.
[50] Brezzi F, Fortin F. Mixed and hybrid finite element methods. Springer-Verlag; 1991.
[51] Arnold D, Brezzi F, Fortin M. A stable finite element for the Stokes equations. Calcolo 1984;21(4):337–44.
[52] Lamichhane B. Inf-sup stable finite-element pairs based on dual meshes and bases for nearly incompressible elasticity. IMA J Numer Anal 2009;29(2):404–20.
[53] Ong TH, Heaney CE, Lee C-K, Liu GR, Nguyen-Xuan H. On stability, convergence and accuracy of bES-FEM and bFS-FEM for nearly incompressible elasticity. Comput Methods Appl Mech Eng 2015;285:315–45.
[54] Areias P, Rabczuk T, César de Sá J. Semi-implicit finite strain constitutive integration of porous plasticity models. Finite Elem Anal Des 2015;104:41–55.
[55] Gekeler E. Mathematical methods for mechanics: a handbook with MATLAB experiments. Springer; 2008.
[56] Green A, Adkins J. Large elastic deformations (and non-linear continuum mechanics). Oxford University Press; 1970.
[57] Elguedj T, Bazilevs Y, Calo V, Hughes T. $\overline{B}$ and $\overline{F}$ projection methods for nearly incompressible linear and non-linear elasticity and plasticity using higher-order NURBS elements. Comput Methods Appl Mech Eng 2008;197(33–40):2732–62.
[58] Ogden R. Non-linear elastic deformation. Dover Publications; 1997.
[59] Destrade M, Saccomandi G. On the rectilinear shear of compressible and incompressible elastic slabs. Int J Eng Sci 2010;48:1202–11.
[60] Angela Mihai L, Goriely A. Positive or negative Poynting effect? The role of adscititious inequalities in hyperelastic materials. Proc Roy Soc A: Math, Phys Eng Sci 2011;467(2136):3633–46.
[61] Logg A, Mardal K-A, Wells G. Automated solution of differential equations by the finite element method. Springer; 2012.
[62] Logg A, Wells G. DOLFIN: automated finite element computing. ACM Trans Math Softw 2010;37(2).
[63] Courtecuisse H, Allard J, Kerfriden P, Bordas S, Cotin S, Duriez C. Real-time simulation of contact and cutting of heterogeneous soft-tissues. Med Image Anal 2014;18(2):394–410.
[64] Hu W, Wu C, Koishi M. A displacement-based nonlinear finite element formulation using meshfree-enriched triangular elements for the two-dimensional large deformation analysis of elastomers. Finite Elem Anal Des 2012;50:161–72.